

Contents

1	Secrets of the nature	1
1.1	The Standard Model	2
1.1.1	Introduction	2
1.1.2	Quantum Field Theory	4
1.2	The Glashow-Weinberg-Salam model	9
1.2.1	Symmetry Breaking mechanism and Goldston theorem	10
1.2.2	Higgs mechanism	11
1.3	Beyond the Standard Model	13
1.3.1	Limitations of the Standard Model	14
1.3.2	Theories beyond the Standard Model	16
1.4	Conclusions	17
2	The ILC	19
2.1	To a linear lepton collider	20
2.1.1	Advantages of a linear lepton collider	20
2.1.2	Future linear lepton collider	21
2.2	The ILC machine	22
2.2.1	Baseline design	22
2.2.2	Machine design and beam parameters	23
2.2.3	Beam backgrounds	25
2.3	The ILC detectors concept	26
2.3.1	Overview of the two experiments	26
2.3.2	Particle flow algorithm	28
2.3.3	The ILD detector	29
2.4	Conclusions	34
3	Physics at the ILC	35
3.1	Potential studies	35
3.2	Higgs physics	37
3.2.1	Production of the Higgs at the ILC	37
3.2.2	Decays of the Higgs	37

3.3	Advantages of the ILC	39
3.3.1	Background processes	39
4	Double-sided VXD: PLUME	41
4.1	The ILD vertex detector specifications	42
4.1.1	Physics requirements	43
4.1.2	Design	44
4.2	PLUME	46
4.2.1	Design and goals	46
4.2.2	Prototypes	46
4.2.3	Perspectives	47
4.3	Integration of CMOS sensors	48
4.3.1	Principle of a CMOS sensor	49
4.3.2	Charges creation and signal collection	49
4.3.3	Signal processing	51
4.3.4	State of the art in high energy physics	54
5	Electrical Validation and laboratory testing	57
5.1	Mechanical check	57
5.2	Electrical validation	57
5.3	Noise estimation	59
5.4	Cluster	59
6	Test beam analysis	61
6.1	Experimental set-up	61
6.2	Deformation studies	61
6.3	Benefits of double-point measurements	61
	Acronyms	63
	Bibliography	65

List of Figures

1.1	Summary of the Standard Model particles with their interactions. http://www.brighthub.com/science/space/articles/84750.aspx	2
1.2	Scalar potential: ADD A GOOD CAPTION.	13
2.1	Schematic layout of the International Linear Collider (ILC).[5]	23
2.2	Representation of the bunch structure at the ILC. One bunch train is made of 2625 bunch crossings and lasts 0.95 ms. Each bunch crossing is spaced out by 337 ns. Two bunch trains are of 0.2s apart from each other.[17]	25
2.3	Overview of the two detectors designs at the ILC. The figure a represents the SiD design while the figure b shows the ILD approach.[6]	27
2.4	Two different approaches for calorimetry. On the left is the traditional calorimetry method used on most of the experiments, the right one is the particle flow approach for calorimetry. The particle track is taken into account to calculate the jet energy.[13]	29
2.5	Quadrant view of the ILD detector concept with its subdetector system [6]	30
3.1	The higgs production processes at the ILC.	37
3.2	The cross section production of the Higgs boson with a mass of 125 GeV. REF HIGGS WHITE PAPER	38
4.1	Overview of the two vertex detector option for the ILC. On the left, it is made of five single sided layers, whereas the right one represents three double-sided layers.	45
4.2	Side view (transversal and longitudinal) of the PLUME mechanical structure.	47

4.3	Drawing of MAPS structure representing the different layers of the sensor and the path of charge carriers in the epitaxial layer.	50
4.4	Two different architectures of pixel. The left one is a pixel of type 3T, whereas the right one is a self-biased one.	52
4.5	Parallel column readout.	53
4.6	Pictures of the STAR vertex detector and an ULTIMATE chip	55
4.7	Layout of the MIMOSA-26 matrix.	55
5.1	Alignment check made with a microscope.	58
5.2	One has to be careful!	58
5.3	Sub-matrix response	59
5.4	TN and FPN	59
5.5	Output of 10k events acquisition with a Fe55 radiation source.	60

List of Tables

1.1	Summary of the 12 fermions. L is a quantum number associated to the leptons. Its value is 1 for leptons and -1 for anti-leptons. B is a quantum number associated to the baryons. It is equal to 1 for a baryon and to -1 for an anti-baryon. [20]	4
1.2	Summary of the interactions and the boson defined by the Standard Model. [20] N.B.: the graviton was not included in this table because the gravitational force is not taken into account in the SM.	5
2.1	Parameters aimed for the silicon tracker using micro-strips sensors.	32
3.1	Summary of the major processes that will be studied at the ILC for different energies[3].	36
4.1	Estimation of the material budget for the different prototypes of the PLUME ladder.	48

Todo list

Conservation laws and invariance	3
Add details on the QED: coupling...	6
Rephrase the section title	9
Yukawa couplings with fermions	13
Paper on ILC	22
Paper on CLIC	22
Draw my one bunch structure figure...	25
Check the table and values....	31
Figure: Feynman diagrams of Higgs production	37
ADD REF TO THE FIGURE	37
Rewrite the introduction... It is not that great dude.	42
REF Marcel VXD	44
REF for a DEPFET paper	45
REF Joel paper	46
Reference to paper from Oleg	48
Figure: Electric sketch	52
Figure: Rolling shutter	53
REF to a paper	54
Figure: Architecture of Mi26	55
Figure: Alignment of two sensors	58
Figure: Wire bounds crashed	58
Figure: Sub-matrix response A.K S-curve	59
Figure: TN and FPN	59
Figure: Output Fe55	60

Chapter 1

Secrets of the nature

In this chapter, we will try to understand the world surrounding us thanks to a mathematical framework which describes the matter and its interaction. We will first have a look at the laws that lead our Universe. Then, we will focus on the mathematical framework with the description of three interactions: the electromagnetism, the weak and the strong interactions. After that, we will study the electroweak interaction and the spontaneous symmetry breaking. We will finally discuss the limits of the theory and the solutions to avoid the limits.

Contents

1.1	The Standard Model	2
1.1.1	Introduction	2
1.1.2	Quantum Field Theory	4
1.2	The Glashow-Weinberg-Salam model	9
1.2.1	Symmetry Breaking mechanism and Goldston theorem	10
1.2.2	Higgs mechanism	11
1.3	Beyond the Standard Model	13
1.3.1	Limitations of the Standard Model	14
1.3.2	Theories beyond the Standard Model	16
1.4	Conclusions	17

1.1 The Standard Model

1.1.1 Introduction

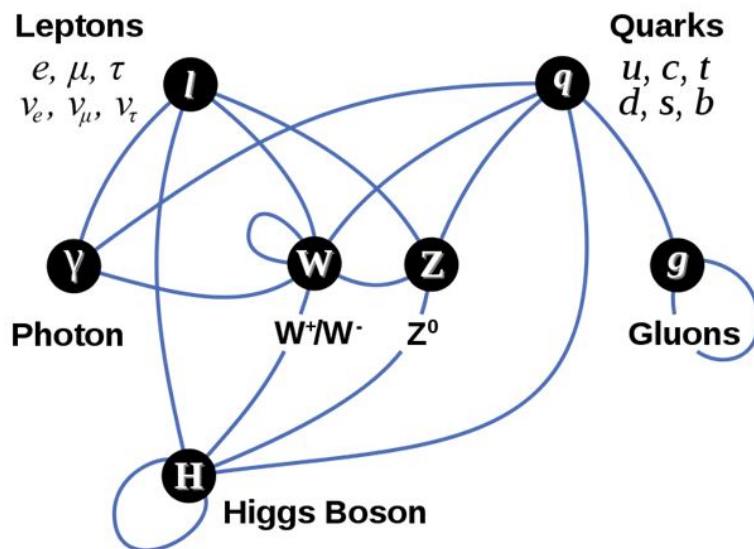


Figure 1.1 – Summary of the Standard Model particles with their interactions.
<http://www.brighthub.com/science/space/articles/84750.aspx>

The Standard Model (SM) is a theory that describes the elementary structure of the matter surrounding us. It is one of the most successful achievements in modern physics. The elegant theoretical framework of the Standard Model (SM) is able to provide good explanations of experimental results but is also able to predict a wide variety of phenomena.

The SM depicts the interactions between the fundamental constituents of matter, called particles. From a quantum point of view, a particle is defined by its intrinsic angular momentum, called spin. This quantum number is a key to distinguish between the particles of 'matter' and the 'carrier force' particles.

The half integers spin particles are obeying to the Fermi-Dirac statistics and are submitted to the Pauli exclusion principle: they can not occupy the

same quantum state at the same time. These particles are called fermions. They are the constituents of the matter and are to the number of twelve.

The fermions are divided into two categories: the leptons and the quarks. The leptons are to the number of six: three charged particles and three neutral particles called neutrino. The first fundamental particle discovered in particle physics was the electron (e^-) at the end of the 19th century. The two other charged leptons were discovered in 1937 for the muon (μ) and in 1975 for the tau (τ). Three neutrinos are associated to the three flavored leptons: the electron neutrino (ν_e) discovered in 1953, the muon neutrino (ν_μ) in 1962 and the tau neutrino (ν_τ) discovered in 2000.

The quarks are to the number of six. They can't be found alone in nature. They are carrying a quantum number: the color. The color quantum numbers are green, blue and red (and the anti-color associated). They are always in a bounded state to form composite particles that are colorless and are called hadrons. A quark and an anti-quark form an integer spin composite particle, a meson. Three quarks bounded together are called baryons. The most known baryons are the proton and the neutron. They are made of the up quarks (u) and the down quarks (d). The other quarks were discovered in the second half of the 20th century. The strange quark (s) was discovered in 1968, followed by the charm quark (c) in 1974. Then, the bottom quark or beauty quark (b) was discovered in 1977. The last quark discovered was the top quark (t) in 1995.

The fermions are also divided into three categories which depend on the mass of the particle. They are called generations. The first generation of particles is composed of the electron, the electron neutrino, the u and d quarks. They form the ordinary matter. The two other generations are particles found in cosmic rays or in collisions with accelerators. All the fermions and their properties are summarised in the table 1.1.

The second kind of particles are integer spins particles and are labelled bosons or gauge bosons. They are following the Bose-Einstein statistics. It means that the bosons are not limited to a single occupancy of the same state as the fermions. The bosons are the mediators of the four fundamental interactions.

Conservation laws and invariance

The electromagnetic interaction (EM) is mediated by the photon γ , a massless and chargeless particle of spin 1. The EM is responsible for the interaction between two charged particles. The weak interaction which is responsible for the β radioactive decay (a nucleon is able to transform into an other one with the emission of a lepton and a neutrino). The gauge bosons associated with the weak interaction are the neutral electrical charged boson Z^0 , and two electrical charged one W^+ and W^- . The strong interaction is mediated by eight gauge bosons, the gluons. It is responsible for the nucleus

Type	Family	Particle	L	B	Q_e	Mass (MeV)
Leptons	1 st	e	1	0	-1	0.511
		ν_e	1	0	0	$< 2 \times 10^{-6}$
	2 nd	μ	1	0	-1	105.66
		ν_μ	1	0	0	$< 2 \times 10^{-6}$
	3 rd	τ	1	0	-1	1.78×10^3
		ν_τ	1	0	0	$< 2 \times 10^{-6}$
Quarks	1 st	u	0	1	2/3	$2.3^{+0.7}_{-0.5}$
		d	0	1	-1/3	$4.8^{+0.5}_{-0.3}$
	2 nd	s	0	1	-1/3	95 ± 5
		c	0	1	2/3	$1.275 \times 10^3 \pm 2.5$
	3 rd	b	0	1	-1/3	$4.66 \times 10^3 \pm 30$
		t	0	1	2/3	$173.21 \times 10^3 \pm 511 \pm 711$

Table 1.1 – Summary of the 12 fermions. L is a quantum number associated to the leptons. Its value is 1 for leptons and -1 for anti-leptons. B is a quantum number associated to the baryons. It is equal to 1 for a baryon and to -1 for an anti-baryon. [20]

and the hadrons cohesion. The last force is the gravitational interaction but it is not included into the SM. Trying to find a framework where the equation of the general relativity used to describe the macro world and the equation of the quantum mechanics describing the micro world is a difficult challenge. From a quantum theory, the boson associated with the gravitational force might be the graviton, a spin 2 particle.

The Higgs boson (H) is a particle predicted by the S.M and has been discovered in 2012 at the Large Hadron Collider (LHC). It is the gauge boson of the Higgs mechanism. This mechanism is the mass generator of particles and will be presented later in section 1.2.2.

The table 1.2 summarises the different bosons of the SM.

1.1.2 Quantum Field Theory

The mathematical basis of the SM is the Quantum Field Theory (QFT). All the interactions are described by the gauge group:

$$SU_C(3) \otimes SU_L(2) \otimes U_Y(1) \quad (1.1)$$

The gauge theory is invariant under a continuous set of local transformation. Taking the gauge symmetries and the least action into account,

Force	Gauge bosons	Mass (GeV/c ²)	Electric charge	Range
Electromagnetic	γ	0	0	∞
Weak	Z^0	91.1876 ± 0.0021	0	10^{-18} m
Weak	W^\pm	80.3980 ± 0.0250	± 1	
Strong	g (8 gluons)	0	0	10^{-15} m
	H	125 GeV	0	

Table 1.2 – Summary of the interactions and the boson defined by the Standard Model. [20]

N.B.: the graviton was not included in this table because the gravitational force is not taken into account in the SM.

physicists were able to set up equations that describe the dynamic of the interactions by Lagrangian. The steps to build Lagrangian for the three forces and the unification of the EM and weak interactions are going to be presented.

Quantum Electrodynamics

The Quantum Electrodynamics (QED) is the QFT that combines the electromagnetism formalism and the quantum mechanics formalism to describe the interaction thanks to a relativistic Lagrangian. As the charge Q_e of the electron is invariant on every part of the Universe, the QED Lagrangian should be invariant under some transformations. The $U(1)$ gauge group is a unitary group of one dimension which is invariant under space transformations.

Lets first consider the Dirac Lagrangian for a free fermion:

$$\mathcal{L}_{Dirac} = \bar{\Psi}(x) (i\gamma^\mu \partial_\mu - m) \Psi(x) \quad (1.2)$$

The Lagrangian is invariant under global U(1) transformation:

$$\begin{aligned} \Psi(x) &\rightarrow \Psi'(x) = e^{-i\alpha} \Psi(x) \\ \bar{\Psi}(x) &\rightarrow \bar{\Psi}'(x) = e^{i\alpha} \bar{\Psi}(x) \end{aligned} \quad (1.3)$$

The corresponding local symmetry is:

$$\begin{aligned} \Psi(x) &\rightarrow \Psi'(x) = e^{-i\alpha(x)} \Psi(x) \\ \bar{\Psi}(x) &\rightarrow \bar{\Psi}'(x) = e^{i\alpha(x)} \bar{\Psi}(x) \end{aligned} \quad (1.4)$$

Although the mass term of the Lagrangian in the equation 1.2 stays invariant under the local symmetry, the term containing a partial derivative is

not anymore. A gauge field A_μ has to be added to the derivative to keep it invariant under local gauge transformation. The covariant derivative will be then:

$$D_\mu \Psi(x) = (\partial_\mu - iQ_e A_\mu) \Psi(x) \quad (1.5)$$

The gauge field is not yet a dynamic field. To get a physical gauge field, a kinetic term should be added to the equation. This gauge invariant term that includes derivative from the A_μ field is:

$$F_{\mu\nu} = \partial_\mu A_\nu - \partial_\nu A_\mu \quad (1.6)$$

The Lagrangian, which is local invariant, is the one that describes the QED:

$$\mathcal{L}_{QED} = \bar{\Psi}(x) (i\gamma^\mu D_\mu - m) \Psi(x) - \frac{1}{4} F_{\mu\nu}(x) F^{\mu\nu}(x) \quad (1.7)$$

A mass term $m A_\mu A^\mu$ for the field A_μ is missing because it is not gauge invariant. That consideration matches to the fact that the photon is a massless boson.

Add details on the QED: coupling...

Weak interaction

In 1930, Pauli assumed that the continuous energy spectrum of the electron in the β decay could be explained by the existence of a new particle to respect the principle of energy conservation. It is a light particle, which does not interact so much with matter.

After the discovery of the neutron by Chadwick in 1932, Fermi wrote a theory on weak interaction to explain the β decay. [11] He postulated that the neutron is decaying into a proton by emitting an electron and a light neutral particle, called neutrino. In analogy to the electromagnetism, he proposed a current-current Lagrangian to describe the β decay.

$$\mathcal{L}_{weak} = \frac{G_F}{\sqrt{2}} (\bar{p}\gamma_\mu n) (\bar{e}\gamma_\mu \nu) \quad (1.8)$$

where the G_F is the Fermi constant $G_F = 1.166 \cdot 10^{-5} GeV^{-2}$.

Nevertheless, the non-relativistic limit leads to an incomplete theory. The interaction considered with a 2-components spinor transforms a proton into a neutron without changing the position, the spin or the parity. However, T.D. Lee and C.N. Yang have postulated in 1956 that the weak interactions violate the parity after analysing the decays of the τ and θ particles[16]. The

Wu experiment [22] confirmed this hypothesis in 1957 by studying the decay of ${}^{60}\text{Co}$.

The Fermi interaction was modified by Feynman and Gell-Mann[12] to a $V - A$ theory¹. The vector current is now subtracted by an axial vector current. For example, the neutrino current is replaced by:

$$\begin{aligned} \bar{e}(x)\gamma_\mu\nu &\rightarrow \bar{e}\gamma_\mu(1 - \gamma_5)\nu \\ &= \bar{e}\gamma_\mu\nu - \bar{e}\gamma_\mu\gamma_5\nu \end{aligned} \quad (1.9)$$

It was established that the weak current has the form $V - A$ instead of $V + A$. The weak interaction is only coupling left-handed particles and right-handed anti-particles.

The lagrangian describing the weak interactions can be written as a currents interaction:

$$\mathcal{L}_{weak} = -\frac{G_F}{\sqrt{2}}J^\mu J_\mu^\dagger \quad (1.10)$$

and J^μ is a combination of leptonic and hadronic currents.

Contrary to the QED, the weak interaction obeys to a non-Abelian symmetry group², the SU(2) symmetry group. The matter field could be represented as a doublet Ψ_L and a singlet Ψ_R of this group.

$$\Psi_L = \begin{pmatrix} \nu_{eL} \\ e_L \end{pmatrix}, \quad \Psi_R = e_R \quad (1.11)$$

The generators of the group are the three Pauli matrices σ_i , associated with a gauge field W_μ^i . The bosons of the weak interactions are the W^\pm and Z .

As the left-handed leptons are combined into a doublet, a quantum number called weak isospin (I_3) is associated with them. The charged leptons have a weak isospin $I_3 = \frac{-1}{2}$ and for the neutrinos $I_3 = \frac{1}{2}$. Concerning the gauge bosons W^\pm and Z , the weak isospin is respectively $I_3 = \pm 1, 0$.

Quantum Chromodynamics

The Quantum Chromodynamics (QCD) is the quantum field theory of the strong interaction. In this model, the interaction is due to an SU(3) gauge group. It produces 8 gauge fields called gluons. The spinors of this theory are the six quarks that form a triplet with respect to the gauge symmetry.

¹ V stands for vector and A for axial-vector

²A group is non-Abelian when the elements of the group are not commutating.

The SU(3) gauge group is a group of $9 - 1 = 8$ real parameters and of 8 generators. Those generators are the Gell-Mann matrices. The normalised generators are defined by:

$$T^a = \frac{1}{2} \lambda^a \quad (1.12)$$

The structure constant f^{abc} can be expressed as:

$$if^{abc} = 2Tr([T^a, T^b]T^c) \quad (1.13)$$

Some theories arguments and the results of experiments in high energy physics have required introducing six spinor fields, the quarks. Each of them is considered as a triplet state with respect to the SU(3) group:

$$q_i = \begin{pmatrix} q_i^1 \\ q_i^2 \\ q_i^3 \end{pmatrix} \quad (1.14)$$

where q_i are the six quarks. These quarks can appear in three different states, called color and that are named red, blue and green.

The local gauge symmetry U(1) should be included into the SU(3) group. The gauge field A_μ can be introduced in the group:

$$A_\mu = g_S A_\mu^a \frac{\lambda^a}{2} \quad (1.15)$$

with $a = 1, \dots, 8$ and corresponds to the 8 gluons. A mass term $m_g A_a^\mu A_\mu^a$ would not be gauge invariant, it implies that the gluons have to be massless.

The covariant derivative is then:

$$\begin{aligned} D_\mu &= \partial_\mu - iA_\mu \\ &= \partial_\mu - ig_S A_\mu^a \frac{\lambda^a}{2} \end{aligned} \quad (1.16)$$

The QED field $F_{\mu\nu}$ is not gauge invariant in QCD. Nevertheless, an additional term to obtain gauge invariant field tensor can be introduced:

$$G_{\mu\nu}^a = (\partial_\mu A_\nu^a - \partial_\nu A_\mu^a) + g_S f^{abc} A_\mu^b A_\nu^c \quad (1.17)$$

Finally, the QCD Lagrangian is given by:

$$\mathcal{L} = \sum_{i=1}^6 \bar{q}_i (i\gamma^\mu D_\mu - m_i) q_i - \frac{1}{4} G_{\mu\nu}^a G_a^{\mu\nu} \quad (1.18)$$

1.2 The Glashow-Weinberg-Salam model

Late 1960, a model of unification was postulated by Glashow, Weinberg, and Salam to describe the electroweak interaction (EW). The theory rests on a $SU(2)_L \otimes U(1)_Y$ symmetry group. It is the simplest group which conserves the properties of EM charge conversion and parity violation of weak interaction.

Rephrase the section title

For the EW unification, the $U(1)_{EM}$ symmetry group describing the EM has to be rewritten. As the fermions are considered by left-handed doublets and right-handed singlets, the $U(1)_{EM}$ will break the gauge invariance. The weak isospin group $SU(2)_L$ is combined with the EM charge to create the hypercharge give by the Gell-Mann-Nishijima relation:

$$Q = I_3 + \frac{1}{2}Y \quad (1.19)$$

The I_3 term is the third component of the weak isospin. With the introduction of the hypercharge, the EM gauge invariance is conserved.

The EW Lagrangian could be given as:

$$\mathcal{L}_{EW} = \mathcal{L}_{YM} + \mathcal{L}_{fermions} ?? \quad (1.20)$$

The first term \mathcal{L}_{YM} is the Yang-Mills Lagrangian that describes the bosons gauges interactions (kinetic term + interaction between bosons). It has the form below:

$$\mathcal{L}_{YM} = -\frac{1}{4}\mathbf{W}_{\mu\nu}^a \mathbf{W}^{a\mu\nu} - \frac{1}{4}\mathbf{B}_{\mu\nu} \mathbf{B}^{\mu\nu} \quad (1.21)$$

With

$$\mathbf{W}_{\mu\nu} = \partial_\mu \mathbf{W}_\nu - \partial_\nu \mathbf{W}_\mu - ig[\mathbf{W}_\mu, \mathbf{W}_\nu] \quad (1.22)$$

$$\mathbf{B}_{\mu\nu} = \partial_\mu \mathbf{B}_\nu - \partial_\nu \mathbf{B}_\mu \quad (1.23)$$

In the equation 1.22, $\mathbf{W}_\mu = \sum W_\mu^i \sigma^i / 2$ is a vector of three gauge fields associated to $SU(2)_L$ and σ^i are the Pauli matrices. The term $[\mathbf{W}_\mu, \mathbf{W}_\nu]$ is associated to the interactions between the gauge fields. In the equation 1.23, \mathbf{B}_μ is the only gauge field associated to the $U(1)_Y$.

The Lagrangian describing the fermions field is given by:

$$\mathcal{L}_{fermions} = \bar{\Psi}_L \gamma^\mu D_\mu \Psi_L + \bar{\Psi}_R \gamma^\mu D_\mu \Psi_R \quad (1.24)$$

$$\text{With } D_\mu \Psi_L = \left(\partial_\mu + ig\mathbf{W}_\mu - i\frac{g'}{2}Y\mathbf{B}_\mu \right) \Psi_L \text{ and } D_\mu \Psi_R = \left(\partial_\mu - i\frac{g'}{2}Y\mathbf{B}_\mu \right) \Psi_R \quad (1.25)$$

In the equation 1.25, the covariant derivative has two forms. The weak interaction does not allow coupling of the W bosons to right-handed fermions whereas the γ and Z bosons do.

With the EW Lagrangian described above, the gauge bosons were considered as massless fields. The electroweak interaction does not allow a $m\bar{\Psi}\Psi$ term because it does not transform as a scalar under $SU(2)_L \otimes U(1)_Y$. Moreover, the $m^2\mathbf{W}_\mu\mathbf{W}^\mu$ violates the $SU(2)_L$ gauge invariance of the Lagrangian. The mass terms associated with the physical fields of the gauge bosons are given by spontaneous symmetry breaking via the Higgs mechanism.

1.2.1 Symmetry Breaking mechanism and Goldston theorem

Before to introduce the Higgs mechanism, we will study the spontaneous symmetry breaking for a global symmetry. This phenomenon is also seen in phase transitions or laser theory.

Let's consider first the Lagrangian density for a complex scalar field ϕ :

$$\mathcal{L} = \partial^\mu \phi^* \partial_\mu \phi - \mu^2 \phi^* \phi - \lambda(\phi^* \phi)^2 \quad (1.26)$$

The first component of the Lagrangian density corresponds to the kinetic term of a complex scalar field, while the second component is related to a scalar potential. The coefficient μ^2 is a real parameter. Nevertheless, depending on its sign, the potential can take two forms.

If $\mu^2 > 0$, the symmetry is unbroken and the potential has a minimum at $\phi = 0$ which does not degenerate. It describes a particle with a mass μ and a quartic self-coupling. As the transformation $\phi \rightarrow -\phi$ is respected, this solution is a symmetric one.

When $\mu^2 < 0$, there is not a unique ground state for this system but multiple states with the same vacuum energy. The minima is located on a circle of radius:

$$v = \sqrt{\frac{-\mu^2}{2\lambda}} > 0 \quad (1.27)$$

By choosing a particular solution as the ground state, the symmetry gets spontaneously broken.

A parametrisation of the excitations around the ground state is possible by introducing a new field ϕ :

$$\phi(x) = \frac{1}{\sqrt{2}} (v + \rho(x) + i\Theta(x)) \quad (1.28)$$

The value v is given by one of the solution from equation 1.32, $\rho(x)$ and $\Theta(x)$ are real fields.

By adding the new field in the equation 1.26, the Lagrangian becomes:

$$\mathcal{L} = \frac{1}{2}(\partial_\mu \rho)^2 + \frac{1}{2}(\partial_\mu \Theta)^2 - \lambda v^2 \rho^2 - \lambda v(\rho^3 + \rho \Theta^2) - \frac{\lambda}{4}(\rho^2 + \Theta^2)^2 \quad (1.29)$$

The field $\rho(x)$ describes a state of mass $m_\rho = 2\mu^2$, coupled to the massless field $\Theta(x)$.

The field $\Theta(x)$ describes excitations around a direction in the potential. The excitations are not costing any energy, so they correspond to massless bosons called Goldstone bosons.

1.2.2 Higgs mechanism

As we have seen with the Lagrangian of the QED and QCD, the bosons generated are massless. Nevertheless, the W^\pm and the Z bosons have a mass and the equation ?? of the EW interaction does not include a mass generator. The origin of the fermions masses is solved in the SM thanks to the Higgs-Englert-Brout mechanism [14][10].

Lets consider first a doublet of complex scalar fields Φ :

$$\Phi = \begin{pmatrix} \phi^+ \\ \phi^0 \end{pmatrix} \quad (1.30)$$

The invariant Lagrangian density under $SU(2)_L \otimes U(1)_Y$ gauge transformation is:

$$\mathcal{L} = (D^\mu \phi)^\dagger (D_\mu \phi) - V(\phi) \quad (1.31)$$

The covariant derivative is the one of $SU(2)_L \otimes U(1)_Y$ given by the equation 1.25 and represents the kinetic term. The Higgs potential is similar to the one considered first and has also two solutions depending on the sign of μ^2 . Let's focus only on the negative solution. There is an infinite set of degenerated states with minimum energy:

$$\phi_0 = \sqrt{\frac{1}{2}} \begin{pmatrix} 0 \\ v \end{pmatrix} \text{ with } v = \sqrt{\frac{-\mu^2}{\lambda}} > 0 \quad (1.32)$$

Let's expand the field Φ around its minima by including a field $h(x)$ which describes quantum fluctuations and three massless Goldstone fields, denoted $\theta^i(x)$:

$$\Phi(x) = e^{i\frac{\sigma_i}{2}\theta^i(x)} \frac{1}{\sqrt{2}} \begin{pmatrix} 0 \\ v + h(x) \end{pmatrix} \quad (1.33)$$

A particular gauge can be defined in a way that the Goldstone fields are absorbed by the physical field of $SU(2)_L \otimes U(1)_Y$. It implies the apparition of mass terms in equation 1.31. First, we are interesting in the mass generation mechanism, we will focus only on the impact of the new field on the derivative covariant, we will omit any h-mixed terms and drop down the partial derivative:

$$\left| \left(i\frac{g}{2}\mathbf{W}_\mu + i\frac{g'}{2}Y\mathbf{B}_\mu \right) \Phi \right|^2 = \frac{1}{8} \left| \begin{pmatrix} gW_\mu^3 + g'B_\mu & g(W_\mu^1 - iW_\mu^2) \\ g(W_\mu^1 + iW_\mu^2) & -gW_\mu^3 + g'B_\mu \end{pmatrix} \begin{pmatrix} 0 \\ v \end{pmatrix} \right|^2 \quad (1.34)$$

The charged fields can be expressed as a linear combination of gauge field:

$$W_\mu^\pm = \frac{W_\mu^1 \mp iW_\mu^2}{\sqrt{2}} \quad (1.35)$$

The eigenstates are rewritten as decorrelated terms representing the neutral fields from the EW symmetry group:

$$Z_\mu = \cos \theta_w W_\mu^3 - \sin \theta_w B_\mu \quad (1.36)$$

$$A_\mu = \sin \theta_w W_\mu^3 + \cos \theta_w B_\mu \quad (1.37)$$

θ_w is the Weinberg angle and represent a bound between the coupling g and g' :

$$\sin \theta_w = \frac{g'}{\sqrt{g^2 + g'^2}} \text{ and } \cos \theta_w = \frac{g}{\sqrt{g^2 + g'^2}} \quad (1.38)$$

The equation 1.34 becomes:

$$\begin{aligned} \left| \left(i\frac{g}{2}\mathbf{W}_\mu + i\frac{g'}{2}Y\mathbf{B}_\mu \right) \Phi \right|^2 &= \frac{1}{8} \left| \begin{pmatrix} A_\mu \sqrt{g^2 + g'^2} & gW_\mu^- \\ gW_\mu^+ & -Z_\mu \sqrt{g^2 + g'^2} \end{pmatrix} \begin{pmatrix} 0 \\ v \end{pmatrix} \right|^2 \\ &= \frac{1}{2} M_Z^2 Z Z^* + \frac{1}{2} M_W^2 W^- W^+ \end{aligned} \quad (1.39)$$

With $M_Z = \frac{1}{2}v\sqrt{g^2 + g'^2}$ and $M_W = \frac{1}{2}vg$, the mass of the Z boson and the W^\pm bosons. The mass of the photon is coherent to the expectation and is null.

The Higgs mechanism implies the existence of a massive gauge field, the Higgs boson. It is coupled to the other bosons and also to itself. This could be shown by extending the Higgs potential with the field defined in equation 1.33:

$$-\lambda v^2 h^2 - \lambda v h^3 - \frac{1}{4}\lambda h^4 \quad (1.40)$$

The first term gives the mass of the Higgs boson, $M_H^2 = 2\lambda v^2$, while the second and third terms are the Higgs self-interactions. The Higgs mass can not be predicted by the theory because it is given by a function of the parameter λ , which is one of the free parameters of the SM.

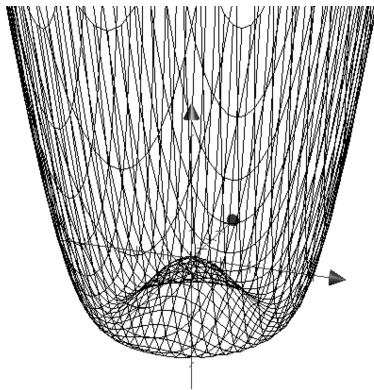


Figure 1.2 – Scalar potential: ADD A GOOD CAPTION.

1.3 Beyond the Standard Model

The SM constitutes one of the most successful achievements in modern physics. One of its strength is to provide an elegant theoretical framework to describe the known experimental facts about particles, but also it was able to predict the existence of a mechanism to generate the particle masses via

Yukawa couplings with fermions

the Higgs mechanism. Nevertheless, a lot of mysteries in the Universe are not explained by this theory.

1.3.1 Limitations of the Standard Model

Despite the fact that the experimental results are not contradictory to the SM, the theory is far away to be the answer to all the questions. The particle physics community is facing a challenge to find the ultimate theory of everything. An exhaustive list of some limitations is going to be presented.

Free parameters

The SM does not explain the existence of the free parameters, which are to the number of 19. It does not explain also why there are three generations of particles and why the gap between generations is spread over five orders of magnitude.

This is not really a problem for the physics itself, nevertheless, the particles physics community has a lack of understanding these values.

Hierarchy problem

The hierarchy problem refers to two main scales problem about the SM.

First of all, the difference between the energy scale of the SM and the Planck scale is of the seventeen orders of magnitude. No "intermediate" physics have been found between the two scale.

A second problem occurs while considering the Higgs boson mass. The SM does not predict its mass, but it sets some theoretical bounds with respect to Λ , the scaled energy at which the SM is not valid anymore. The theoretical Higgs mass is higher than what it should be compared to the EW scale. The Higgs interacts with the particles of the SM (fermions, W and Z boson), but it also interacts with himself. Due to the scalar nature of the boson, they are quartic divergences while calculating the loop corrections. The quantum corrections, which take into account the coupling of the Higgs, are Λ^2 divergent and lead to a huge Higgs mass. To avoid that, delicate cancellations should occur between the quantum corrections. These cancellations are known as the fine-tuning problem.

Gravitation

Although particles physicists are dreaming of a "theory of everything" that will unify the electroweak, strong and gravitational interactions, there is no

viable theory to describe the gravity in a quantum point of view to include it in the SM and which would be still valid at a macro-scale.

Neutrino mass

The neutrinos defined by the SM are assumed to be exactly massless. Nevertheless at the end of the 90's, the Super Kamiokande experiment had surprising results. There was a lack on the expected solar and atmosphere neutrinos flux. The result was interpreted by an oscillation of neutrinos between the three leptonic flavors. However, the oscillation is possible only if the neutrino has a mass. That phenomenon could be considered as a proof of physics beyond the SM.

Matter-antimatter asymmetry

As discussed at the beginning of this chapter, the SM defines an equal number of particles and anti-particles. Although everyone assumes that the matter and antimatter were created in an exactly equal amount by the Big Bang, a mechanism has favoured electrons, protons, and neutrons to positrons antiprotons and antineutrons. If the amount of matter and antimatter was equal, our Universe would have been completely annihilated. The matter domination could be a local phenomenon with an antimatter surrounding the region. However, the region of contact between matter and antimatter would be a violent place of interaction, which would disturb the cosmic microwave background.

An assumption to explain the asymmetry is that the antimatter was produced in an infinity proportion compared to the matter. Hence, the annihilation as lead to create a Universe only made of matter. A mechanism which tends to prefer the matter has been observed in the study of the kaon oscillation. This particle is able to transform spontaneously to its own anti-particle and vice-versa. Nevertheless, this transformation is not symmetric: the kaon is slower to turn into an antikaon than the inverse transformation. Unfortunately, the SM provides no explanation about that mechanism.

Dark Matter

Several astrophysical observations are indicating that the Universe is made not only of visible matter but also of matter that seems to be invisible to the electromagnetic interaction, the dark matter. In 1933, a measurement of the galaxies velocities in the Coma cluster to determine the cluster mass gives a surprising result. The mass was more than two orders of magnitude bigger than the mass of visible stars in the cluster. It was found that the matter of

the SM describes only 5% of the Universe content. The rest of the Universe is made of 22% of dark matter and around 73% of dark energy. The neutrinos are possible candidates to dark matter, as it couples to SM matter via only weak interaction, but they cannot account for the entire density of the universe. Nowadays only twelve particles (plus the anti-particles associated) have been observed. The idea of dark matter comes from the way we estimate the mass of a galaxy is estimated.

1.3.2 Theories beyond the Standard Model

Supersymmetry

The Supersymmetry (SUSY) is a QFT, that relates the elementary fermions known to corresponding bosons, called sfermions and the bosons to corresponding fermions, sbosons [21]. The related particles are called super-partners. They have the same mass, the same quantum numbers but the spin is differing by a half factor. SUSY might be a broken symmetry. This will allow the super-particles to acquire very high masses.

SUSY is a good candidate for physics beyond the SM. It will solve the hierarchy problem without any fine tuning. For example, the loop contributions of one particle to the Higgs are cancelled by the loop contributions of its super-partner. It will be able to provide a framework for the unification of the three gauge interactions at a GUT scale. The lightest super-particle is a good candidate for the Dark Matter.

Despite it will answer many questions from the SM, there is a lack of understanding why SUSY is a broken symmetry.

Grand unification theory

After the success of the electroweak unification, the next step is to include the strong interaction to build the Grand Unification Theory (GUT), an extension of the SM. In this framework, the three forces are different manifestations of a single interaction. It includes the $SU(3)_C \otimes SU(2)_L \otimes U(1)_Y$ symmetry group into a larger $SU(5)$ group. The quarks and leptons are ordered in left decuplets and right quintets. The coupling constants are described by only one parameter. There are 24 mediators, the 12 mediators of the SM plus 6 X mediators (charge $\pm 4/3$ and 3 colors) and 6 Y mediators (charge $\pm 1/3$ and 3 colors). It predicts the existence of new particles as leptoquarks³, multiple Higgs bosons and new currents.

Unfortunately, the theory is not validated because of its prediction of the proton lifetime. The first GUT was introduced by Georgi and Glashow in

³Coupling between a lepton and a quark

1974 and was predicting a decay of the proton. The actual experimental limit of the proton lifetime is set to 5×10^{32} years, whereas the predicted lifetime defined by the SU(5) group is one order of magnitude lower. [20]

Technicolor

The technicolor is a theory that explains the mass generation. Contrary to the EW symmetry, the masses of particles are not generated by the spontaneous symmetry breaking but they are generated by a strong gauge interaction. This interaction is strong and confined at the energy that has been experimentally probed. The approach of the theory avoids the hierarchy problem induced by the SM.

String theory

The particle physicists have the dream of unifying the forces of the nature to have only one single interaction with four different manifestations. The string theory proposes a framework for the "theory of everything". The basic unit of matter is no more considered as particles but a one-dimensional string of which particles are various vibrational modes.

The string theory is a theory of quantum gravity. It tries to unify the gravitation to the quantum Extra dimensions of 10 -11 space-time dimensions. Possible explanation for the hierarchy problem.

1.4 Conclusions

We have seen the beauty and the limits of the SM. The high energy physics community is trying to study as far as possible the limit of the SM and is also trying to find some proof of new physics beyond the SM. The (LHC) at CERN has permitted in 2012 to point out the existence of a Higgs boson. Nevertheless, the beam structure of the LHC is not efficient enough to perform very precise measurements. Because of the collision between protons, the energy of the collision can't be exactly known. The next chapter deals with a future experiment in high energy physics, where electrons and positrons are used to probe the matter instead of protons and antiprotons.

Chapter 2

The future of high-energy physics: the International Linear Collider

Since 2008, the Large Hadron Collider (LHC) is actually the most powerful tool in high-energy physics to have a better understanding of the universe, particularly with the discovery in 2012 of a new particle compatible to the boson predicted by the spontaneous symmetry breaking of the SM [1, 8]. Although the LHC is an impressive machine able to reach the highest energy scale of collision available on Earth with a centre-of-mass energy of 13 TeV, the complex environment of the events generated hides the access to some fundamental parameters. To achieve more precise measurements of the Higgs boson, but also to test the validity of the SM and other physics theories introduced in the chapter 1, the high energy physics community has merged on the necessity to build a linear electron-positron collider, that will work as a complementary accelerator to the LHC.

This chapter will explain the motivations to invest a huge amount of money in a new great world project. It will present the complementary nature of the lepton and hadron colliders and the main advantages of the lepton collisions will be discussed. After giving an overview of the ILC with its basic design and the experiment models, we will focus on the design of one of the detectors: the International Large Detector (ILD).

Contents

2.1	To a linear lepton collider	20
2.1.1	Advantages of a linear lepton collider	20
2.1.2	Future linear lepton collider	21
2.2	The ILC machine	22
2.2.1	Baseline design	22

2.2.2	Machine design and beam parameters	23
2.2.3	Beam backgrounds	25
2.3	The ILC detectors concept	26
2.3.1	Overview of the two experiments	26
2.3.2	Particle flow algorithm	28
2.3.3	The ILD detector	29
2.4	Conclusions	34

2.1 To a linear lepton collider

The most impressive accelerator ever built is located at CERN in Geneva, Switzerland. It is the world largest particle accelerator, with a circumference ring of nearly 27 kilometers, straddling the Swiss and French borders. It is designed to collide two counter rotating beams of protons or heavy ions, with a possibility to reach centre-of-mass energies of 13 TeV with a high peak luminosity of $10^{34} \text{ cm}^2\text{s}^{-1}$. The goals of the LHC are to perform further tests on the SM, search for new forces or produce dark matter candidates. Indeed, the collider covers a wide energy range at the constituent level while running at a fixed beam energy. Unfortunately, due to the nature of the particles used, the experiment can not reach the highest precision measurements needed.

Complementary to a discovery machine such as the LHC, a machine to perform precise measurement should be built: the linear lepton collider.

2.1.1 Advantages of a linear lepton collider

First of all, during each collision at an hadron collider, only a part of the total centre-of-mass energy is available for the process evolved, therefore the initial four-vector momentum is not known. By colliding leptons, which are structureless objects, the full centre-of-mass energy is available for the elementary process. The initial four-vector momentum of an interaction is exactly known, hence the event can be fully reconstructed.

Secondly, with a lepton collider, the beam energy is tunable and both electron and positron beams can be polarised. The selection of an appropriate polarisation can boost the signal and suppress the background cross-section.

Thirdly, as seen in the first point, at the LHC, only a fraction of the partons are contributing to the interesting process. The proton-proton interaction cross section is dominated by inelastic background QCD processes. The signal event is then accompanied by large backgrounds produced by the

interaction of other parton collisions. This background masks the elementary process of interests, in order that it has an impact on the detector design, that should have a high radiation tolerance and implement a selective trigger to reduce the data rate. The lepton colliders do not suffer from this kind of background and at similar energies, the event rate is lower as those of hadron colliders. Moreover, the interaction of electrons and positrons is purely electroweak. In consequence, the detector does not have to handle extreme data rates and can be used without any trigger. Hence, the sensitivity to any possible signature of new physics is improved.

Although the leptons, in particularly the electron and positron, have clearer advantages on hadrons to perform a precise measurement, the choice of a linear collider comes from the physics of accelerating charged particles. While charged particles are moving in a circular accelerator, they lose some energy by emitting photons via synchrotron radiation. The equation 2.1 describe the energy loss via synchrotron radiation:

$$\Delta E_{sync} \sim \frac{E^4}{m^4 r} \quad (2.1)$$

The radiative energy loss is proportional to the radius r of the accelerator, the energy of the particle E to the power of the fourth and its mass m to the power of the fourth. As the electron mass is $\sim 1.8 \times 10^3$ smaller than the proton mass, the energy loss radiated by the electron is bigger than the energy loss radiated by proton at the same centre-of-mass energy. To compensate the energy loss, a circular electron-positron accelerator should have an extremely big radius (bigger than the actual LHC), increasing the cost to build the experiment. Another solution to overcome the synchrotron radiation is to accelerate the particles in a linear collider. Nevertheless, the centre-of-mass energy has to be reached in only one path, whereas the bunch of particles in a circular collider is accelerated many times in the ring until the desired energy of collision is reached. To still get an "affordable" experiment, the centre-of-mass energy obtained at a linear collider is below to the one from a circular collider. Indeed, to work at the same energy scale, a linear collider would require a bigger number of accelerating cavities and would make a much bigger and more expensive collider than a circular one.

2.1.2 Future linear lepton collider

As it was mentioned before, the precise measurements offered by lepton collider is one of the key points to constrain the limits of the SM and to characterise precisely all the known particles. Since the 1980's, several linear collider technologies have been developed, leading in the 1990's to five major accelerator technologies: Superconducting Radio-Frequency (SRF), the

Paper on ILC

Paper on CLIC

Compact LInear Collider (CLIC) technology and three different normal conducting technologies (S-band, C-band, and X-band)[9]. At the beginning of the 2000's, a committee for the future linear collider was formed and has chosen in 2004 the SRF technology[15] and since then all the efforts are done in that direction to build the International Linear Collider (ILC). The technology developed for this future experiment is also used for the XFEL at DESY in Hamburg and at KEK in Japan. Another linear collider project led by the CERN is being prepared: the CLIC. It has a more challenging technology to aim a nominal energy of 3 TeV instead of 1 TeV for the ILC. Contrary to the ILC, CLIC plans to use radio-frequency structures and a two beam concept. Another idea would be to develop a muon collider instead of electron-positron collider[18]. As the electron, the muon is a pointlike particle, therefore the centre-of-mass energy can be easily adjusted to perform a precise study. The muon mass is 207 times much bigger than the electron ones and suffers less of energy loss by synchrotron radiation. Hence, a circular collider could be more adapted and the beamstrahlung effects would be smaller in a muon collider than in an e^+e^- machine. Nevertheless, the muon has a lifetime of only $2.2\ \mu s$ making up a more challenging acceleration design.

For the purpose of this thesis, the CLIC and muon colliders will not be described more to focus on details on the ILC.

2.2 The ILC machine

The ILC should be the next lepton collider experiment and will be situated in Japan. During 2016, the physicists community is waiting for an official decision of the Japan government concerning final site where the experiment will be held. At the time this thesis was written, the most likely site candidate is located in the north of Japan, in the region of Kitakami.

2.2.1 Baseline design

The ILC is planned to collide electrons and positrons at a center-of-mass energy up to 500 GeV, with an energy variability down to 200 GeV for 31 kilometers long accelerator. An upgrade to reach the centre-of-mass energy of 1 TeV is also possible, but the accelerator should be extended to achieve a total length of 50 kilometers. It is designed to generate a total of $500\ fb^{-1}$ of data during the first four years of operation. The luminosity will reach a peak of $2 \times 10^{34}\ cm^{-2}s^{-1}$ at $\sqrt{s} = 500\ GeV$.

The main components of the ILC are presented in the following order: first of all, an overview of the electron source and their acceleration via the conducting and superconducting structures, then the role of the damping

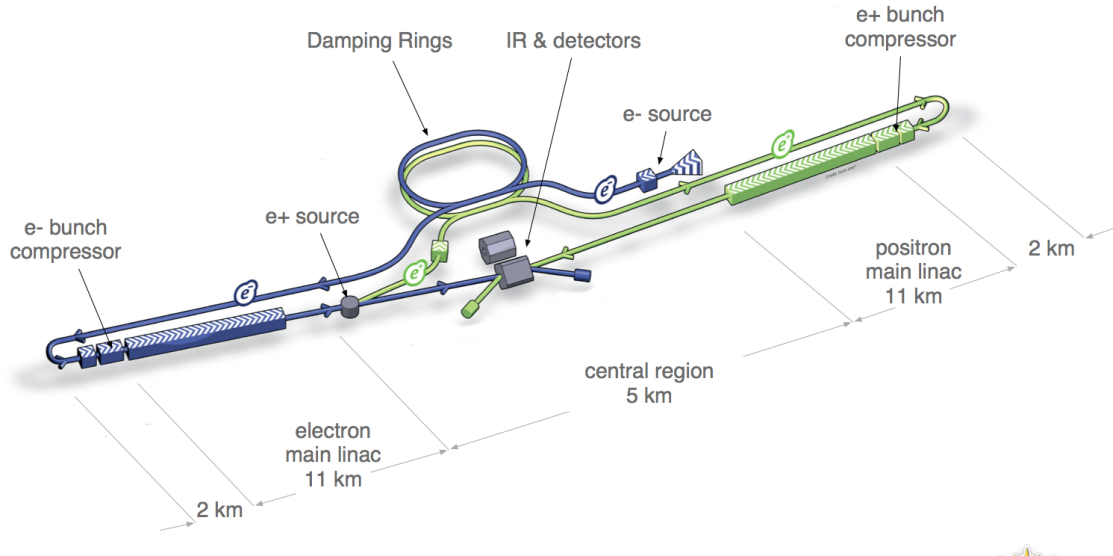


Figure 2.1 – Schematic layout of the International Linear Collider (ILC).^[5]

rings, the injection into the main linacs, followed by the positron source and the Beam Delivery System (BDS) to finally present the interaction region (IR). A detailed description of the ILC could be found in the Technical Design Report^[2].

2.2.2 Machine design and beam parameters

The polarised electrons are produced by a laser firing a strained GaAs photocathode in a Direct-current (DC) gun. To implement a redundancy, the electron generation system is made of two lasers and DC guns, providing bunches with a polarisation of 90 %. The electrons are then pre-accelerate to 76 MeV thanks to non-superconducting accelerating structures. Thereafter, they are injected into a 250 m long superconducting linac to reach the energy of 5 GeV. Nevertheless, the dimension and density of bunches are quite extended, thus their emittance is too wide. Before to inject the bunches into a damping ring, which is used in order to decrease the emittance and reach the desired luminosity, superconducting solenoids rotate the spin vector into the vertical direction, while SRF cryomodules are used for an energy compression.

The damping ring is 6.7 km length and made of magnets and wrigglers that are going to force the particles to get a bent track. This system is used to dump the electrons with large transverse and longitudinal emittance to

the low emittance required for the luminosity production. The reduction of the emittance should be achieved within 200 ms between the machine pulses. Although the positron source was not yet introduced, their bunches suffer from the same problems as the electron ones. A second damping ring, placed in the same cavern as the electron one, is also in charge to get the desired emittance.

The bunches are then extracted from the damping rings and transferred via the Ring To the Main Linac (RTML) structure, the longest continuous beam line at the ILC. It is divided into five subsystems to transport the bunches from the damping rings to the BDS, in order to orient the beam in the desired polarisation by rotating the spin of the particle, but also to compress the beam bunch length from several millimeters to a few hundred microns thanks to a two-stage bunch compressor. At the same time the bunches are compressed, sections of SRF technology accelerate the bunches from 5 GeV up to 15 GeV. One of the challenges of the RTML is to preserve the emittance obtained after the damping rings, while the length and the energy of the bunches are tunned. Then, the particles are delivered to the main Linac, an 11 km long accelerator using 1.3 GHz SRF cavities, made of niobium.

Before to reach the interaction region, the primary electron beam is transported through a 147 m superconducting helical undulator to produce photons from ~ 10 up to ~ 30 MeV, depending on the energy of the primary beam. This primary beam is separated from the photons and sent back to the BDS with an energy loss of ~ 3 GeV. The photons are directed onto a rotating Ti-alloy target to create e^+e^- pairs that are separated. The positrons collected are accelerated to 125 MeV thanks to a normal conducting linac and then accelerated to 5 GeV with a superconducting boost linac. Finally, they are introduced into the damping ring to reduce their emittance.

The two beams are transported from the high energy LINACS to the IR by the BDS, in charge to focus the beams to the sizes required to meet the ILC luminosity wanted. It is divided into five main subsystems. First, in the direction of the beam, a system is in charge to perform some emittance measurement and matching, to give a trajectory feedback, and provide a polarimetry and energy diagnostic. Then the beam is collimated to remove the beam-halo particles that would generate a huge amount of background in the detector. Muons generated during the collimation process are deflected by magnetised iron shielding. Thereafter, strong compact quadrupoles focus the beam to the sizes required to meet the desired luminosity. Before the collisions, crab cavities rotate the bunches in the horizontal plane for effective collisions and to achieve a 14 mrad total crossing angle. After the collisions, an extraction line is dedicated to transport the beams into the main beam dump.

Although two experiments will run at the ILC, there will be only one interaction region due to cost reasons. Indeed, to have two experiments running at the same time, it requires two separate BDS of 4 km long each. Thanks to a push-pull scheme, the detectors will work alternatively: while one is taking data, the other one is sitting in the garage to be maintained. The two detectors will be presented in more details at section 2.3.

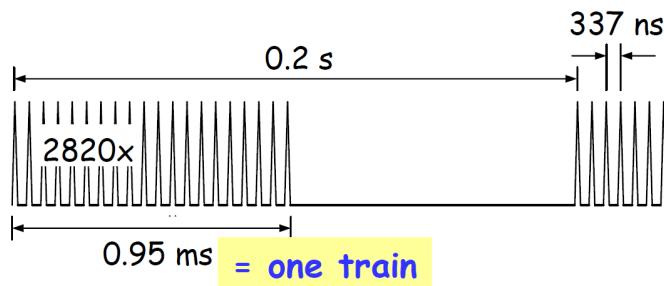


Figure 2.2 – Representation of the bunch structure at the ILC. One bunch train is made of 2625 bunch crossings and lasts 0.95 ms. Each bunch crossing is spaced out by 337 ns. Two bunch trains are of 0.2s apart from each other.[17]

The accelerator described above will create bunch trains at a repetition rate of 5 Hz. Each train is composed of 2625 bunches that contain 2×10^{10} particles and lasts 0.95 ms. The interval between two trains is 2 ms long. This structure is a feature key to develop detectors able to be switched off during the dead time in order to reduce the power consumption.

Draw my one bunch structure figure...

2.2.3 Beam backgrounds

To design the detectors of the ILC, the backgrounds must be understood and taken into account to give optimal performances. The event reconstruction becomes more complicated with hits caused by background particles. They are two kinds of background, the one created by the BDS and the one related to the interaction point. As it was discussed in the subsection 2.2.2, the collimator placed closed to the interaction point (IP) to purify the beam can produce muons by an electromagnetic shower. To sweep them away, iron spoilers are used to create a magnetic field and deflect the muons. A side effect is to increase the number of neutrons created in photo-nuclear

reactions. A concrete wall placed at the entrance of the experimental hall vanishes the neutron background.

Contrary to the LHC, the ILC will not suffer from the QCD background, as mentioned in subsection 2.1.1 Nevertheless, due to the nature of electrons and positrons, the two beams will interact each other before they collide. The electromagnetic beam field of each bunch is high and causes the focusing of the opposite bunch. It is bending the electron/positron trajectories near the IP. On the one hand, this effect helps to focus the incoming beams and enhance the luminosity. On the other hand, as the charged particles have bending track, they are emitting hard photons via beamstrahlung, creating e^+e^- pairs background. The hard photon is strongly focused in the forward region and do not contribute strongly to the background in the detector. However, the e^+e^- pairs created contribute to the background directly or through backscattered particles. In consequence of the beamstrahlung, the beam particle energy is reduced, hence the collisions occur at different energies from the nominal one and this affects the physics cross-section. The beamstrahlung photons can also produce neutrons by hitting components. The other source of hard photons is the initial state radiation. With the beamstrahlung, they contribute reducing the luminosity[19].

Different kinds of soft pairs background can be expected at the ILC: the coherent and incoherent pair production. The coherent pair production appears when beamstrahlung photons are interacting with the strong electromagnetic field of the beams. In the ILC environment the coherent pair background are negligible, whereas the incoherent pair production is dominant. It corresponds to e^+e^- pairs created by the interaction of only two particles. They are to the number of three depending on the nature of the scattered photons creating the e^+e^- pair. The Bethe-Heitler process corresponds to the scattering of one real photon while the second one is virtual. It contributes to approximately two of the third pair production. The second process is the Landau-Lifshitz, where the two scattered photons are virtuals and contribute to approximately to the third of the pair creation. The last production occurred via two real photons (Breit-Wheeler process) and contribute only to a percent level. The incoherent e^+e^- pairs are produced at a relatively low transverse momentum and are emitted in the forward direction.

2.3 The ILC detectors concept

2.3.1 Overview of the two experiments

As it was presented in the subsection 2.2.2, the ILC will be built with only one interaction region due to cost reasons, whereas two detectors are expected.



(a) The Silicon Detector



(b) The International Large Detector

Figure 2.3 – Overview of the two detectors designs at the ILC. The figure **a** represents the SiD design while the figure **b** shows the ILD approach.[6]

The push-pull operation scheme will allow for data taking of one detector, while the second one is out of the beam in a close-by cavern for maintenance. The interval to switch the detectors should be short enough and of the order of one day. This time efficient implementation sets specific requirements for the beam structure but also for the detector design. The detectors should be placed on platforms to preserve the alignment and to distribute the load equally onto the floor. Another requirement on the detector design is that the magnetic fields outside the iron return yokes must be small enough to not disturb the second detector on the parking position. It is assumed that a limit of 5 mT at a lateral distance from the beam line should be sufficient.

The motivation to build two detectors with a different approach is mainly to provide a cross-checking and a confirmation of results and complementary strengths. Both detectors are optimised to study a broad range of preci-

sion measurements and search of new physics drove by the ILC expectations. Their performances are driven by the Particle Flow Algorithm (PFA) to be able to measure the final states of events with a high accuracy. To do so, both detectors should have a high hermeticity, high granularity calorimeters and excellent tracking and vertexing. The PFA is shortly presented on subsection 2.3.2.

The Silicon Detector (SiD) is a compact detector made of a silicon tracking and 5 T magnetic field. The tracking system should provide robust performance thanks to the time-stamping on single bunch crossings. The calorimeters should be highly granular to perform the PFA.

The second detector is the ILD. In contrast to the SiD, the tracking system is based on a continuous readout Time-Projection-Chamber (TPC) surrounded by silicon tracking detectors. The magnetic field will be only of 3.5 T combined with granular calorimeters for a good particle-flow reconstruction

2.3.2 Particle flow algorithm

The main purpose of the ILC (or the CLIC) is to achieve precise measurements of physics processes that produce final states with multiple jets. The jet energy resolution at the ILC should be sufficient to cleanly separate W and Z hadronic decays. Typically, the jet energy resolution is deduced from the equation 2.2, where α is the stochastic term usually greater than $\sim 60\%/\sqrt{E(GeV)}$.

$$\frac{\sigma_E}{E} \simeq \frac{\alpha}{\sqrt{E(GeV)}} \oplus \beta \quad (2.2)$$

The PFA approach is the extended version of the Energy Flow approach (used at H1, D0, CMS) for a highly granular detector. The goal of this framework is to achieve a stochastic term for the energy resolution greater than $30\%/\sqrt{E(GeV)}$, not reachable with a traditional calorimeter. Each sub-detector should be efficient enough to separate and to reconstruct the four-vectors of all visible particles in an event. The energy of charged particle is measured in the tracking detectors, while the energy measurements for photons are done in the electromagnetic calorimeter and neutral hadrons are done in the hadron calorimeter.

The PFA requirements drive the design of the detectors at the ILC. For both experiments, the electromagnetic and hadronic calorimeter have to be located inside the solenoid. Moreover, each sub-detector must be able to distinguish single particle signals, imposing a better tracking precision and

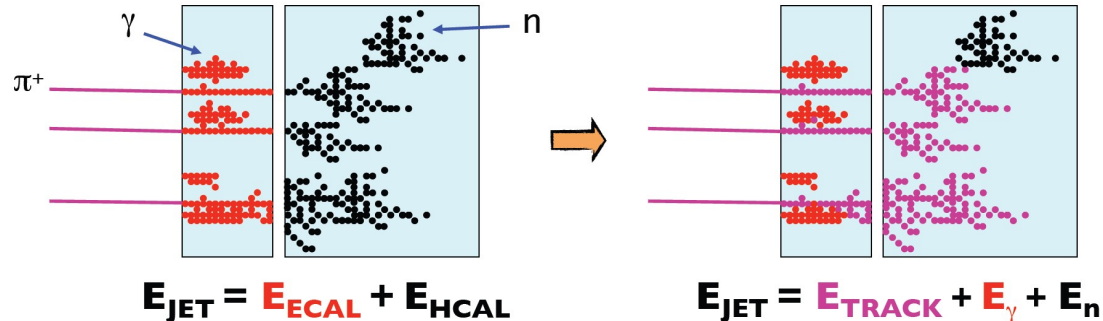


Figure 2.4 – Two different approaches for calorimetry. On the left is the traditional calorimetry method used on most of the experiments, the right one is the particle flow approach for calorimetry. The particle track is taken into account to calculate the jet energy.[13]

higher granular calorimeters than the traditional detectors in high energy physics.

2.3.3 The ILD detector

The design of ILD follows the requirements for optimal PFA performance. In summary, the detector should be highly granular to have a robust three-dimensional imaging capability. It will combine a high-precision Vertex Detector (VXD) system, a hybrid tracking system and calorimeters inside a 3.5 T solenoid. On the outside, a coil and iron return yoke will be instrumented as a muon system and a tail catcher.

Vertex detector

The chapter 4 will introduce in more details the vertex detector requirements for the ILD (material budget and precision of measurements) and the different design proposals. For the moment, two designs are under study for the vertex detector, but both of them has a pure geometry barrel. The first one is made of five single sided layers and the other one three double-sided detection layers.

Tracking

The main tracking system for the ILD is performed by the TPC. It is a gaseous detector with a low material budget designed to measure the particles' trajectory. When a particle traverses through the TPC, it ionises the

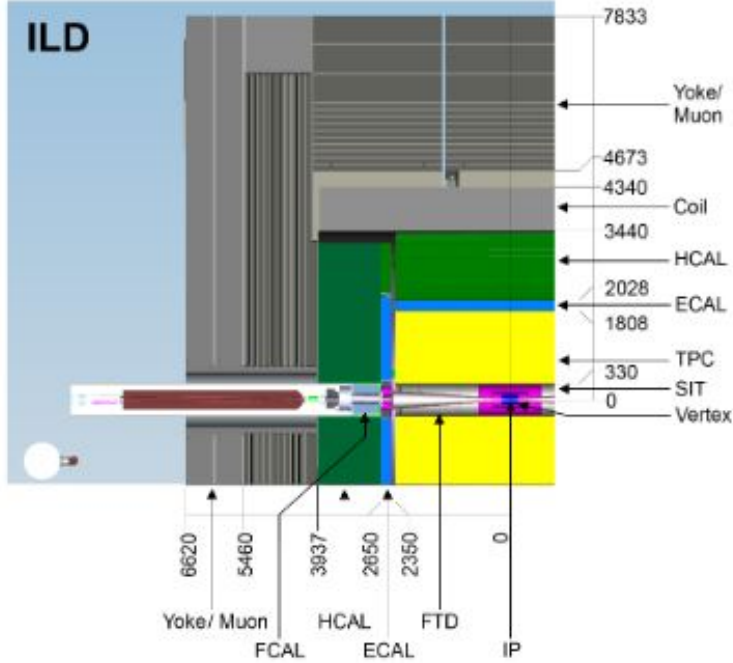


Figure 2.5 – Quadrant view of the ILD detector concept with its subdetector system [6]

gas, creating electrons that are drifting to the anode thanks to a high voltage. The anode is the part where the readout plates are installed. It provides a 3D position of the particles tracks thanks to the wires and the anode (give x-y) and the z coordinate is given by the drifting time. In addition to the exact position measurement, this detector is also able to measure the energy $\frac{dE}{dx}$ deposited by the particle and would be the first step for a particle identification.

The requirements to design a TPC at the ILC are given by two main values:

- The single point resolution $\sigma_{s.p.}$ which should be lower than $100 \mu\text{m}$ in the $r\phi$ direction and less than $500 \mu\text{m}$ in the z direction;
- The minimum distance to separate two hits which should be lower than 2 mm.

The TPC thought for the ILD is constituted of a central barrel part, with an inner radius of $\simeq 33 \text{ cm}$ and a outer radius of $\simeq 180 \text{ cm}$ and two

endcaps with a detection area of 10 m^2 . The solid angle coverage is up to $|\cos \theta| \simeq 0.98$. The barrel will be filled with a gas mixture called T2K (3 % of Ar-CF₄ and 2 % of isobutane). Due to the low material budget and the ability to cope with a high magnetic field, the TPC is compliant with the PFA 2.3.2.

To improve the track reconstruction, the TPC is surrounded by high silicon detectors: two barrel components, the Silicon Internal Tracker (SIT) and the Silicon External Tracking (SET); an end-cap component, the Endcap Tracking Detector (ETD) and the Forward Tracking Detector (FTD). The SIT is linking the tracking between the VXD and the TPC, whereas the SET is giving an entry point to the Electromagnetic CALorimeter (ECAL) after the TPC. Both systems provide precise space points and improve the overall momentum resolution. The goal of the SIT is to improve the momentum resolution, the reconstruction of low p_T charged particles and the reconstruction of long-lived particles. The coupling of the SIT and SET provide also a time-stamping information.

The ETD is located within the gap separating the TPC and the endcap calorimeter. It improves the momentum resolution for charged tracks with a reduced path in the TPC. It also reduces the effect of the material of the TPC end-plate. The material budget of this end-plate is estimated to 15 % of X_0 .

As the TPC does not provide any coverage in the forward region, seven silicon disks ensure efficient and precise tracking down to very small angles, whereas the ETD and the FTD make sure to get a full tracking hermeticity.

To simplify the system layout and the maintenance, the SIT, SET and ETD are made of single-sided strip layers tilted by a small angle with respect to each other. They are placed in a so-called false double-sided layers. The SIT has two layers of microstrip, instead of one layer for the SET. The technology studied are microstrip sensors with an area of $10 \times 10 \text{ cm}^2$, with a pitch of $50 \mu\text{m}$, a thickness of $200 \mu\text{m}$ and an edgeless. The dead area of the sensors will be reduced down to few microns instead of $100 \mu\text{m}$. The spatial point resolution aimed for this detectors is $\sim 7.0 \mu\text{m}$ in the $r\phi$ direction. The table 2.1 gives the single point resolution aimed, as well as the angular coverage and the material budget.

The FTD is placed in the forward direction, between the beam pipe and the inner field cage of the TPC, where the magnetic field becomes less and less useful to bend charged tracks and so the determination of a precise momentum is more difficult. It consists of seven tracking disks: the two firsts are pixel detectors to cope with expected high occupancies and the five others are strip detectors. The pointing resolution will vary between $3.0 - 6.0 \mu\text{m}$ for the two firsts layers and $7.0 \mu\text{m}$ for the five other ones.

Check the table
and values....

Detector	Single point resolution (μm)	coverage	material budget X_0 (%)
SIT	$\sigma_{R-\phi} = 7.0$ $\sigma_Z = 50.0$	$\cos \theta \sim 0.91$	0.65
SET	$\sigma_R = 7.0$	$\cos \theta \sim 0.79$	0.65
ETD	$\sigma_X = 7.0$	$\cos \theta \sim 0.799 - 0.985$	0.65

Table 2.1 – Parameters aimed for the silicon tracker using micro-strips sensors.

Calorimeters

The calorimeters design is driven by the particle flow requirements. Each particle must be reconstructed individually in the detector with a jet energy measurement equal to:

$$\frac{\Delta E}{E} = 30\% / \sqrt{\frac{E}{\text{GeV}}} \quad (2.3)$$

The energy resolution obtained in equation 2.3 is obtained thanks to a combination of information from the tracking system and the calorimeters. The choice of technology used for the calorimeter will be determined by the pattern recognition performance. One of the ILD detector's goal is, for example, to be able to get a jet energy resolution sufficient to clean separate W and Z hadronic decays.

The average jet energy distribution is roughly:

- 62% of charged particles (mainly hadrons)
- 27% of γ
- 10% of long-lived neutral hadrons
- 1.5% of ν

The ECAL is the first calorimeter right after the tracking system. Its role is to identify photons and leptons and measure their energy, nevertheless, it is also the first section to develop the hadron showers. The fine segmentation makes an important contribution to hadron-hadron jet separation. For the ILD, a compromise between the performance and the cost has led to use a sampling calorimeter realised with tungsten absorber. There are three options under study for the active area. The first one called SiW-ECAL, is made of silicon pin diodes with a pitch of $5 \times 5\text{mm}^2$. It has the advantage to cover a large area, to be reliable and simple to operate, to have thin readout layers and can be operated in 3.5 T magnetic field. The second option is made

of scintillator strips readout by photo-sensors and is called ScECAL. It has an active area of $5 \times 45\text{mm}^2$ arranged in alternative directions to achieve an effective granularity of $5 \times 5\text{mm}^2$. The weakness of this technology happened in dense jets environment, where the reconstruction becomes more and more complicated. Some alternatives are also thought, like the Micromegas chambers. Nevertheless, this technology is less advanced compared to the others. One other good candidate could be the use of Monolithic Active Pixel Sensor (MAPS) sensors. They have the advantage to get the signal sensing and processing on the same substrate and by choosing standard CMOS processes, the cost of fabrication would be reduced.

The HAdronic CALanalogue HCALorimeter (HCAL) has the role to separate the deposits energy of charged and neutral hadrons and to precisely measure the energy deposited. It is also a sampling calorimeter using stainless steel instead of tungsten as an absorber. The rigidity of stainless steel makes possible to get a self-supporting structure limiting the dead areas. Two baseline technologies for the active medium area are studied. The Analogue HCAL (AHCAL) is made of scintillator tiles, whereas the semi-digital, called Glass Resistive Plate Chamber (RPC), is based on the Semi-Digital HCAL (SDHCAL).

In order to monitor the luminosity and the beamstrahlung, the calorimeter system is completed in the very forward region by three different subsystems covering very small angles also for neutral hadrons: the LumiCal, the BeamCAL, and the Low angle Hadron CALorimeter (LHCAL). The LumiCAL is placed in a circular hole of the end-cap ECAL and covers polar angles between 31 and 77 mrad. It serves as luminosity monitor by measuring the Bhabha scattering $e^+e^- \rightarrow e^+e^-$ via emission of virtual γ . Indeed, the luminosity \mathcal{L} is determined by measuring the ratio of the number of counted events N_B in a considered polar angle ranged and the integral of the differential cross-section σ_B in the same region. The measurement precision should be better than 10^{-3} at 500 GeV. After each bunch crossing, the beamstrahlung pairs hit the BeamCal. This would permit to get an estimation of the bunch-by-bunch luminosity, but also to determine the beam parameters. It is placed in front of the final focus quadrupole and covers polar angles between 5 and 40 mrad. The third system, the LHCAL, ensure the coverage of the hadron calorimeter to small polar angles.

Magnetic Field and yoke

By applying a high magnetic field inside the detector, the charged particles have a bent track helping in the identification and the energy measurement. At the ILD, the nominal magnetic field is 3.5 T and should have a high homogeneity inside the TPC. Moreover, as mentioned in subsection 2.2.2,

the magnetic beyond the coil has to be reduced to avoid any perturbations with the second detector in its parking position. A superconducting coil surrounding the tracking and calorimetric system generate the magnetic field. It has a diameter of 6.88 m, a length of 7.35 m and made of three modules.

Surrounding the coil, an iron yoke ensures to return the magnetic flux. It is constituted by a barrel of 2.88 m thickness and 2 end-caps of 2.12 m thickness. Muon detectors are inserted inside the iron yoke in a sandwich-like structure. They're performing measurement on muons but they are also used as tail catchers, to improve the energy resolution of high energetic jets escaping the calorimeters.

2.4 Conclusions

In this chapter, the reasons to build a linear electron/positron collider were discussed by introducing the pros and cons of such a big experiment. In order to reduce the costs, only one interaction region is planned but two detectors are going to operate alternately. The design of the detectors is driven by the particle flow approach to reach a ... energy resolution. In particularly, the onion structure of ILD was peeled. The different sub-detectors and the technology options were introduced, except for the vertex detector. Indeed, the chapter 4 will be dedicated to the vertex detector at the ILD.

The next chapter will introduce the physics cases at the ILC, especially by describing an approach to a physics analysis to study the $H \rightarrow c\bar{c}$.

Chapter 3

Physics at the ILC

In the chapter 1, the framework of particles physics was described. Since the beginning of High Energy Physics, different experiments have been done to confirm the exactness of the SM but also to find new physics beyond the SM. The beam structure allow different kind of measurements. For example, the LHC has a high luminosity and high energy beam, able to reach new energy scale on earth, whereas the ILC is trying to reach more precise results, with less energy. This chapter will discuss the physics that will be studied at the ILC. It will focus particularly on the Higgs physics. An introduction to a physic analysis will be given.

Contents

3.1	Potential studies	35
3.2	Higgs physics	37
3.2.1	Production of the Higgs at the ILC	37
3.2.2	Decays of the Higgs	37
3.3	Advantages of the ILC	39
3.3.1	Background processes	39

3.1 Potential studies

As seen in chapter 2, the ILC will have a vast and variable tunable centre-of-mass energy. Due to the features of an e^+e^- collider, the initial state of collision is well defined. Contrary to the LHC, there are no strong interaction backgrounds and the electroweak background is controlled and calculable.

This conditions will help to perform precise measurements and looking for new physics.

For example, the ILC will be able to collect more Z boson events than the LEP did at the centre-of-mass energy $\sqrt{s} = 91$ GeV. It will allow to perform ultra precise measurements of the Z boson and the electroweak sector to study the Z asymmetries and couplings, but also to measure rare processes that were limited by statistics at LEP.

By increasing the centre-of-mass energy to $\sqrt{s} = 160$ GeV, ultra precise measurements of the W mass could be performed (MeV precision) and with higher energy, it is also possible to measure precisely the W boson couplings. Also, at higher energy, there is a new perspective to measure precisely the nature of the Higgs boson and its coupling. The large statistics given by the ILC will permit to study rare Higgs decay.

Top physics

New physics

Energy (GeV)	Reaction	Physics Goal
91	$e^+e^- \rightarrow Z$	ultra-precision electroweak
160	$e^+e^- \rightarrow WW$	ultra-precision W mass
250	$e^+e^- \rightarrow Zh$	precision Higgs coupling
350 - 400	$e^+e^- \rightarrow t\bar{t}$	top quark mass and couplings
	$e^+e^- \rightarrow WW$	precision W couplings
	$e^+e^- \rightarrow \nu\bar{\nu}h$	precision Higgs couplings
500	$e^+e^- \rightarrow ff$	precision search for Z'
	$e^+e^- \rightarrow t\bar{t}h$	Higgs coupling to top
	$e^+e^- \rightarrow Zh h$	Higgs self-coupling
	$e^+e^- \rightarrow \tilde{\chi}\tilde{\chi}$	search for supersymmetry
700-1000	$e^+e^- \rightarrow AH, H^+H^-$	search for extended Higgs states
	$e^+e^- \rightarrow \nu\bar{\nu}hh$	Higgs self-coupling
	$e^+e^- \rightarrow \nu\bar{\nu}VV$	composite Higgs sector
	$e^+e^- \rightarrow \nu\bar{\nu}t\bar{t}$	composite Higgs and top
	$e^+e^- \rightarrow t\bar{t}^*$	search for supersymmetry

Table 3.1 – Summary of the major processes that will be studied at the ILC for different energies[3].

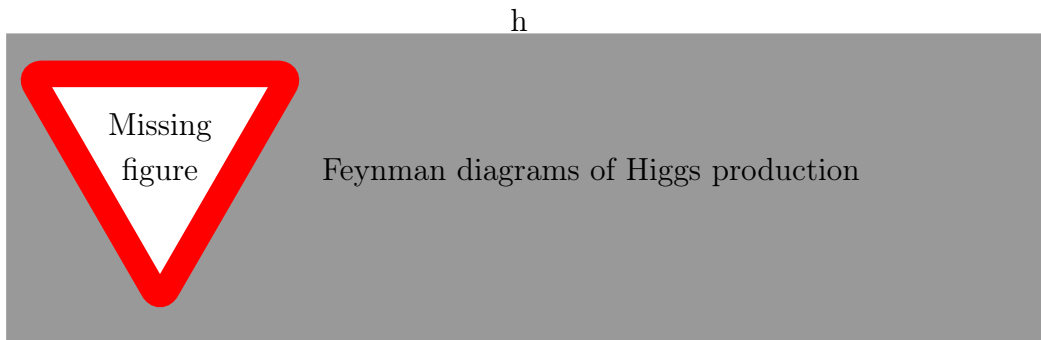


Figure 3.1 – The higgs production processes at the ILC.

3.2 Higgs physics

3.2.1 Production of the Higgs at the ILC

Contrary to the LHC, the Higgs will be accessible by direct measurement. They are three major processes Higgs boson production at the ILC, the Higgs-strahlung, the WW-fusion and the ZZ-fusion:

Higgs-strahlung: $e^+e^- \rightarrow ZH \rightarrow f\bar{f}X$

WW-fusion: $e^+e^- \rightarrow \nu\bar{\nu}W^+W^- \rightarrow \nu\bar{\nu}H$

ZZ-fusion: $e^+e^- \rightarrow e^+e^-ZZ \rightarrow e^+e^-H$

The Higgs-strahlung is a s-channel process that is dominant at 250 GeV and its cross-section falls off as $1/s$ as the centre-of-mass energy \sqrt{s} increases. The WW-fusion and ZZ-fusion are t-channel processes. The cross-section grows logarithmically with the center-of-mass energy and the contribution of the fusion processes is small at 250 GeV.

The polarisation of the beam will help the experimenters to select Higgs reactions or to change the mixture of signal and background. For example, the WW-fusion occurs only with left-handed electrons associated to right-handed positrons.

The figure shows the cross-section production of the Higgs at the ILC
regard to the energy of the collision.

ADD REF TO
THE FIGURE

3.2.2 Decays of the Higgs

The Higgs boson couples to all the particles of the SM. There are many decay modes: $b\bar{b}$, WW , ZZ , gg , $c\bar{c}$, $\tau\tau$, $\gamma\gamma$, γZ . At the LHC, the decay $h \rightarrow b\bar{b}$ can

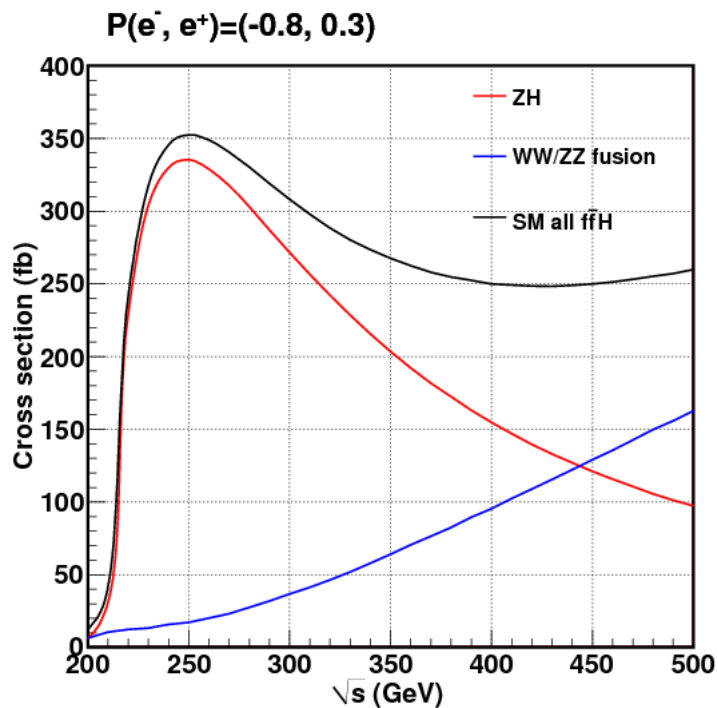


Figure 3.2 – The cross section production of the Higgs boson with a mass of 125 GeV. REF HIGGS WHITE PAPER

be observed with special kinematics but the $h \rightarrow c\bar{c}$ and $h \rightarrow gg$ decays are extremely challenging to observe.

3.3 Advantages of the ILC

The ILC has the main advantage to produce events non accessible at the LHC. Through this section, some benefits of the ILC are introduced thanks to a simple analysis of simulated data at 350 GeV.

The goal of this section is to present how to perform an analysis from simulated data. Measuring the Higgs coupling to $c\bar{c}$ is important to have a reference value to understand any deviations from the SM predictions in the Higgs coupling to $t\bar{t}$ and gg . To study this coupling, the analysis will focus on the final state that gives two neutrinos and two jets coming from the Higgs.

3.3.1 Background processes

They are many background to take into account:

Chapter 4

Double-sided VXD: PLUME

The aim of the ILC is to perform precise measurement of new and already known particles. It can be achieved only by a proper detector design, driven by flagship measurements like the Higgs coupling to quarks and bosons. In fact, the complex events generated at the LHC hide the possibility of a direct measurement of the Higgs. The vertex detector at the ILC should be able to perform an efficient B-meson tagging and to separate b and c quarks. The measurement of heavy quark jets and their decay vertices will play a crucial role in the ILC physics. Along this chapter, the role of the vertex detector and the physics requirements to build one suited for the ILC will be presented. Then, the different options for the ILD are shown to focus on the double-sided options developed by the PLUME collaboration. To finish, the principle of Complementary Metal Oxide Semi-conductor (CMOS) sensors and their use in physics are described.

Since the 1970's, the development of position sensitive silicon radiation sensors has permitted to confirm the prediction of the SM with a high precision, as well as the discovery of the t quarks. To perform precise measurement at the ILC to discover new particles or to characterise more accurately new ones, the VXD has to be built with respect some flagship measurements. For example, to study the coupling of the Higgs with the quarks and bosons, this detector has to be able to separate efficiently the b quarks to the c quarks.

At the ILC flagship measurements such as the Higgs coupling to the quarks and bosons are driving the development of the vertex detector. For example, to separate b (1.3 10-12)and c (1.1 10-12)quarks To measure particles with a short life-time ($\simeq 10^{12}$ s) that have a decay length between 150 and 500 μm ,

The sub-detector has to be able to separate particles with a time life $\simeq 10^{-12}\text{s}$

The ILC is aiming to perform more precise measurements of new and

Rewrite the introduction... It is not that great dude.

already known particles.

Contents

4.1	The ILD vertex detector specifications	42
4.1.1	Physics requirements	43
4.1.2	Design	44
4.2	PLUME	46
4.2.1	Design and goals	46
4.2.2	Prototypes	46
4.2.3	Perspectives	47
4.3	Integration of CMOS sensors	48
4.3.1	Principle of a CMOS sensor	49
4.3.2	Charges creation and signal collection	49
4.3.3	Signal processing	51
4.3.4	State of the art in high energy physics	54

4.1 The ILD vertex detector specifications

Motivations: flavour tagging and lifetime measurements via secondary and tertiary vertex finding. To measure lifetime in picosecond regime one needs a spatial resolution of the order of 5-300 microns. Typical parameters are thickness, pitch, and resolution.

The VXD is the closest sub-detector to the IP in charge of reconstructing the vertex by extrapolating particles back to their origin of production. This detector should be optimised to track particles in a high-density environment and to able to extract the tracks from the different kind of particles, especially the b and c quarks in the case of the ILC. The reconstruction of the displaced vertices should be efficient enough to perform a good flavour tagging. The minimum distance of the first VXD layer is determined by the background induced by beamstrahlung. This sub-detector has a central role in track reconstruction. Depending on the option chosen, the VXD has to provide five or six points of measurement with very high precise spatial resolution. For the studies requiring vertex charge identification, it should be able to reconstruct low-momentum and very forward tracks.

4.1.1 Physics requirements

The ideal VXD should be made of sensors with a fine granularity in order to increase the ability to distinguish two nearest particles. The mechanical structure of the detector should provide a good stiffness and stability of the whole system but has to be at the same time as light as possible to reduce the interaction of the particles traversing it before they reached another part of the main detector. As well, in order to reduce the unwanted interactions, the sensor technology used has to have a low power consumption to avoid any special cooling system which can have a bad impact on the material budget. The design of the such a detector, like the minimal distance of the first layer to the IP and the spacing between different layers, is determined by both the beam background and the physics to study. The flavour tagging ability, the vertex charge measurement and tracking and the displaced vertices reconstruction are the main physics parameter driving the design. The distance of closest approach of a particle to the colliding beam is called the impact parameter and the resolution achievable by the detector is described by the formula 4.1[4].

$$\sigma_{IP} = a \oplus \frac{b}{p \sin \theta^k} \quad (4.1)$$

The first term a is the impact parameter resolution of the sensors used for the VXD, which is linked up to the radii of the inner R_{int} and outer R_{ext} layers and the single point resolution $\sigma_{s.p.}$.

$$a = \sigma_{s.p.} \frac{R_{int} \oplus R_{ext}}{R_{ext} - R_{in}} \quad (4.2)$$

In the case of the ILD, the single point resolution should not be higher than $\sigma_{sp} \simeq 3\mu\text{m}$, leading to an impact parameter with a resolution of the order of $a \simeq 5\mu\text{m}$. The second term is related to the multiple scattering which induces an incertitude on the impact parameter. It depends on the charge Z of the impinging particle, the material crossed by the particle $\frac{x}{X_0 \sin \theta}$ and the distance of the innermost layer to the IP. Depending on the momentum or the crossing angle of the incoming particles, the two parameters are more or less important. For low momentum particles or crossing particles with a shallow angle, the b parameter becomes important, while for higher momentum a dominates.

It the dominant parameter for low momentum particles or particle crossing the sub-detector with a

$$b = R_{int} \frac{13.6 MeV/c}{\beta c} Z \sqrt{\frac{x}{X_0}} \left[1 + 0.036 \ln \left(\frac{x}{X_0 \sin \theta} \right) \right] \quad (4.3)$$

For the ILC purpose, the ILD-VXD should reach an impact parameter resolution better than $5 \mu\text{m}$ and a b parameter better than $10 \mu\text{m GeV}/c$. The values were never obtained before for other experiments. As a comparison, the resolution parameters for the LHC are: $a = 12 \mu\text{m}$ and $b = 70 \mu\text{m GeV}/c$.

4.1.2 Design

The VXD is made of ladders arranged cylindrically in concentric layers to form long-barrels surrounding the IP, contrary to the SiD vertex detector where the design is based on a 5 layers barrel, four endcap disks and three additional forward pixel disks. Two different geometries are competing for the ILC-ILD, nevertheless, they aimed to build long ladders. The first option is based on five single-sided layers, whereas the second one is based on three double-sided layers. The material budget to be reached is 0.11 % of X_0 per layer for the single-sided option and 0.16 % of X_0 per layer for the double-sided. The radius of the first layer depends strongly on the beam background as it is the first layer which is the most impacted. For the single-sided option, the idea is to have five layers with a radius range from 15 to 60 mm. The material budget per layer should be better than 0.1 % of X_0 . The second option is made of three double-sided layers with a radii range from 16 to 60 mm. The material budget for each detecting face should not exceed 0.16 % of X_0 . At the moment the mechanical structure that holds the two layers is 2 mm thick, but some geometry optimisation depending on the physics to study might consider having closer layers on the first ladder, while the last ladder could have a thicker mechanical structure.

REF Marcel
VXD

Both geometry designs are embedding pixel sensors instead of strips or any other silicon devices. A non-exhaustive list of the technologies under competition are presented below:

FPCCD

The Fine Pixels Charged Coupled-Device (FPCCD) [7] is based on the Charged Coupled-Device (CCD) processes. The sensor is using small pixels $\sim 5 \mu\text{m}$ to provide a sub-micron spatial resolution and an excellent capability to separate two nearby tracks. Its thickness is $50 \mu\text{m}$ and the epitaxial layer ($15 \mu\text{m}$ thick) is completely depleted to limit the charge spread around pixels and reduce the number of hit per pixels. However, the CCD architecture provides slow readout and the matrix will be read between consecutive bunch

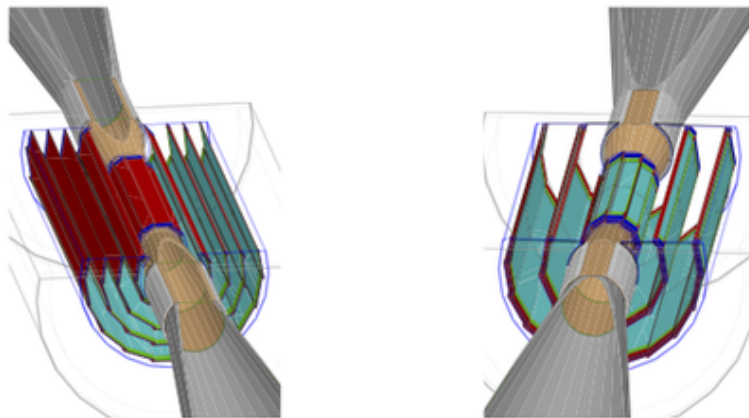


Figure 4.1 – Overview of the two vertex detector option for the ILC. On the left, it is made of five single sided layers, whereas the right one represents three double-sided layers.

trains, helping to reduce the power consumption and avoiding beam induced RF noise. At the moment, the FPCCD are operated at minus forty degrees Celsius.

DEPFET

The Depleted P- Channel Field Effect Transistor (DEPFET) is a Active Pixel Sensor (APS) in which field effect transistors are incorporated into each pixel. The single point resolution is $\sim 3 \mu\text{m}$ for pixels with a size of $20 \mu\text{m}$. The silicon itself is used as sensitive part but also as a support structure, minimising the support and services. The sensor is completed depleted of free charged carries thanks to a voltage applied to the thickness. The rolling-shutter approach is used for reading each row and the column readout is done by two auxiliary Application-Specified Integrated Circuits (ASICs).

REF for a
DEPFET paper

CMOS

A third option is the integration of CMOS pixel sensors. The STAR experiment at RHIC is the first one to get an entire vertex detector made of ULTIMATE-MIMOSA28 CMOS sensors. One of the technology developed is described in section 4.3.

4.2 PLUME

The Pixelated Ladder with Ultra-low Material Embedding (PLUME) project aims to produce double-sided ladder prototypes with respect to the ILC requirements. The collaboration is involving three labs in Europe: the IPCH-PICSEL of Strasbourg, the University of Bristol and the DESY in Hamburg. All together, the collaboration is studying the feasibility to build such vertex detector using MAPS thinned down to $50\mu\text{m}$ and is exploring the benefits of this design. Strasbourg is in charge to develop and mount the sensors on the modules, to take care of the readout and the Data AcQuisition (DAQ), the cooling system. The mechanical design, stability measurements and building the ladders are done by the University of Bristol, while DESY studies the ladder mock-up, performs some power pulsing tests and is testing the modules in the lab. The test beam was mainly done by Strasbourg until I've started yeah!

4.2.1 Design and goals

The figure 4.2 illustrates the design of a PLUME ladder. The mechanical structure is made of a 2 mm thick silicon carbide foam which has a density varying between 8% for the prototype build before 2011 and 4% for the new ones. The choice of this foam is a good compromise between the stiffness and the thickness compare to other materials. It is macroscopically uniform and has the advantage to be easily machinable. Nevertheless, it has a low thermal conductivity (50 W/m/K) and can't be used to dissipate the heat. On each side, a low mass flex-cable is glued to power and to manage sensors from outside, via a connector on one edge. It is made of copper traces (prototype before 2011) or aluminum traces (new prototypes) coated in Kapton. The ladder embeds twelve sensors, six on each face, that are glued and connected to the flex cable. At the moment, the design is dedicated to the MIMOSA-26 sensors thinned down to $50\mu\text{m}$ but it could evolve into any kind of MAPS sensors having the same thickness. Although the MIMOSA-26 has a spatial resolution better than $3\mu\text{m}$, the integration time is not suited for the bunch train structures of the ILC.

REF Joel paper

The aims of the collaboration are to build ladders with a material budget better than 0.35 % of X_0 for a spatial resolution better than $3\mu\text{m}$.

4.2.2 Prototypes

Before to reach the lightest ladder with a material budget of only 0.35 %, the collaboration has studied the design, production and impact of the mechanical structure, but also how to power and control the sensors.

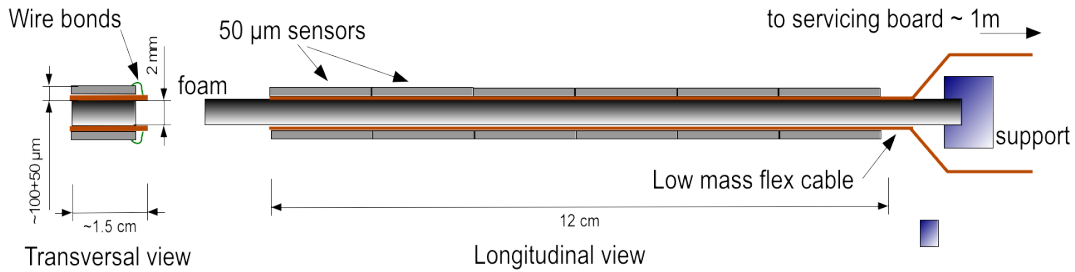


Figure 4.2 – Side view (transversal and longitudinal) of the PLUME mechanical structure.

The first ladder prototype (here labelled V0) was developed and test in 2009. It has two MIMOSA-20 analog output sensors on each side of a stiffener, providing a $1 \times 4 \text{ cm}^2$ sensitive area. As the purpose of this prototype was to settle the fabrication and the beam test procedure, the sensors and the flex-cables were not optimised.

The second prototype featuring the final device design (V1) was developed in 2010. The material budget is estimated to be 0.65 % of X_0 in the sensor's sensitive area. It is the first version to embed six MIMOSA-26 binary output sensors on each side of the stiffener that were working simultaneously. Two ladders were tested, one with 120 GeV pions at CERN-SPS in 2011 and the second one with positrons up to 5 GeV at DESY. The test beam at DESY is presented in chapter ... and some results of sensor's deformation observed at CERN are discussed in chapter ...

The third prototype was mounted at the beginning of 2016 and has not been yet tested. The traces thickness was reduced, the flex-cable width was adjusted to the sensors width and the stiffener was made of a lower density Silicon Carbide foam reducing the material budget and the dead areas.

4.2.3 Perspectives

Although the collaboration has shown their expertise to build light mechanical structures, more tests and optimisations have to be done. MIMOSA-26 sensors are not designed to match the ILC specs. The integration time of this sensor is 115.2 μs , whereas the bunch train last only 0.95 ms (bunch crossing spaced out by 337 ns), a new CPS with a faster integration time has to be built. Although some tests were performed to used the power pulsing on the Mi-26 in order to decrease the power consumption, these sensors can't

Layer	budget (% X ₀)		
	V0	V1	Goal
Sensor	0.053	0.053	0.053
Flex-cable	0.524	0.150	0.034
Passive components	0	0.033	0.033
Stiffener (foam)	0.764	0.175	0.087
Total	1.926	0.654	0.334

Table 4.1 – Estimation of the material budget for the different prototypes of the PLUME ladder.

Reference to paper from Oleg

be used for that purpose.

The collaboration has to perform power pulsing test in a strong magnetic field to study the impact of the Laplace forces on the ladder and also the impact of the power pulsing on the capacity of the sensors.

4.3 Integration of CMOS sensors

The PICSEL group of the IPHC of Strasbourg is developing since 1999 CMOS sensors called MIMOSA for *Minimum Ionizing MOS Active pixel sensor*. They are semi-conducting pixel sensors based on the APS, an alternative to the CCD developed at the beginning of the 1990's by the imaging industry and used nowadays for the smartphone's cameras. One particularity of the sensors developed by Strasbourg is that the different region of the sensor, such the sensitive area or the electronic layer where the signal is processed, are made of the same material. Such device is called then MAPS and the different layers are:

- A substrate used as a bulk;
- An epitaxial layer which is the sensitive volume of the sensor;
- An electronic layer where are located the diodes collection charges and the microelectronic that is processing the signal.

The motivation to use this technology or any other silicon sensor in particle physics is due to the minimum energy needed to create an electron/hole pair by a traversing particle. In silicon, this minimum energy is only 3.6 eV, while for a gaseous detector, it is close to 30 eV.

4.3.1 Principle of a CMOS sensor

When a particle is traveling through matter, it loses energy via interaction with electrons and nuclei. For a thin layer of material, particles can cross all of the environment and lose a small fraction of their energy. It is admitted that Minimum Ionizing Particle (MIP) creates 80 e- per microns. For thin layer, energy loss is described by a Landau while thick material by a Gaussian.

4.3.2 Charges creation and signal collection

At the beginning, the microelectronic industry has insulated the transistors from the substrate thanks to a high resistivity layer, called the epitaxial layer. The development of CMOS sensors was done thanks to the properties offered by these semiconductors.

The different structure of the sensor has different doping. The bulk is a P++ doped layer made with a moderate quality silicon. The crystal structure has high defect crystal structure leading to a high rate recombination of charge carriers. Above the substrate, the epitaxial layer is P-doped and made of a good quality silicon. The electron/hole pairs created in this layer do not recombine instantaneously like in a highly doped layer but they are thermally drifting.

The CMOS sensors developed by the IPHC of Strasbourg are called monolithic MAPS sensors because the different layers of the sensor are made in one block of the same material. The structure of the sensor is highly doped P+ substrate made of a moderate quality silicon. It means that there are a lot of defaults in the crystal structure. This implies a high recombination rate of charge carriers. Above the bulk a layer made of good quality silicon to avoid the recombination of the charge carriers is grown. It is low-doped P- and is called epitaxial layer. It is the sensitive part of the sensor. On top of the epitaxial layer, an N-well implant has the role of the charge collection. The junction between the N-wells and the epitaxial layer create a P-N junction. At this junction, a depleted area is created that attracts the charge carriers. Nevertheless, this P-N junction is only one part of the pixel. Next to the N-wells implants are sitting highly doped P-well that reflects the charge carriers to the N-wells implants. The difference of doping between the bulk and the epitaxial layer is also used to reflect charge carriers to the collection implants.

The typical doping concentration are 10^{15} at/cm³ for the epitaxial layer, 10^{19} at/cm³ in the substrate and 10^{17} at/cm³ for the other layers. The doping concentration defines the size of the depleted region.

As no external voltage is applied to the sensor to increase the depleted region, the charge carriers by particles are thermally diffused inside the sen-

sitive volume to the diode. Nevertheless, the different doping concentration produces a built-in voltage defined as:

$$V_b = \frac{kT}{q} \ln \left(\frac{N_{p+}}{N_{p-}} \right) \quad (4.4)$$

The built-in voltage depends on the Boltzmann constant k , the temperature T , the elementary charge q and the different concentrations doping $N_{p\pm}$ of the interface. The charge collection efficiency is different from a fully-depleted sensor. Indeed, the thermal diffusion

Charge carriers thermally diffused, their average path in epitaxial layer is longer than the one they would have in a fully-depleted sensor. It is more likely that charge carriers are recombining in a nondepleted sensor. The charge collection efficiency is

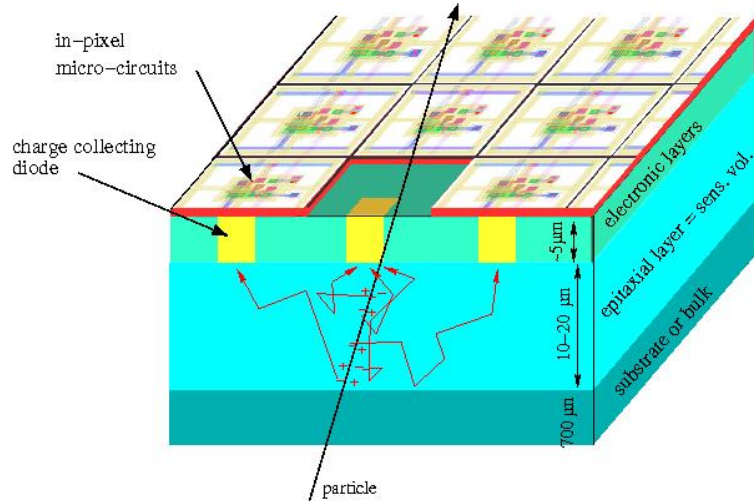


Figure 4.3 – Drawing of MAPS structure representing the different layers of the sensor and the path of charge carriers in the epitaxial layer.

The CMOS sensors have several interesting properties. As this technology uses industrial process, the cost of fabrication is lower than other pixel technologies not based on an industrial process. It allows to build many prototypes and build big matrix sensor. It also benefits from the industrial experience. The CMOS technology is using smaller and smaller grid size (or more granular matrix). A pitch size of ten microns can be achieved. As it was discussed before, due to the property of the small depleted area, the charge carriers tend to spread more over pixels. On the one hand, the signal is smaller per pixel, but the spatial resolution reconstructed with a centre of

gravity algorithm is increasing. For example, binary output sensors with a pitch of $18.4 \mu\text{m}$ can achieve a spatial resolution better than $3 \mu\text{m}$.

Another interesting property is coming from the doping of the different layers. The bulk is not entirely responsible for the charge carriers reflection, only the interface between the substrate and the epitaxial layer is mainly responsible for the reflection. The substrate can be thinned down to few microns leading to a sensor with a thickness of $50 \mu\text{m}$ while keeping the possibility to manipulate them. The material budget can then be reduced to 0.053 %.

As the epitaxial layer is thin, the signal collected by the diodes is small. A MIP is creating 80 electron/hole pairs per microns, so the pixels are collecting between 1000 to more electrons.

CMOS sensors are sensitive to ionizing and non-ionizing radiations that degrade the sensor properties. The non-ionizing radiations are damaging the crystal structure of the epitaxial layers, creating defaults in the lattice. The recombination rate is increasing and reduces the signal collected. To avoid this effect, two solutions are possible. The first one is to reduce the size of the pixels to decrease the path of the particles from the epitaxial layer to collection diodes. Nevertheless, the cost to build sensors with a smaller pitch is increasing. The second solution is to increase the resistivity of the epitaxial layer to increase the depleted area.

The ionizing radiations are responsible for charges accumulation in the electronic layer. The leakage current is increasing in the pixel and diode collection. To reduce the leakage current, smaller diodes can be used to reduce the impact of the leakage current but as it was explained before, the cost of fabrication is increasing.

4.3.3 Signal processing

If no charge is collected by the pixel, the voltage at the equivalent capacitor of the diode is evolving because of the leakage current inherent in the junction. The pixel reading can be done in two different ways, depending on the method used to minimise the leakage current effect. Currently, two pixel's architectures are used to compensate the diode's leakage current: the *3 Transistors pixel design*, mainly used in imaging, and the *self-biased pixel design*. The circuit diagram which is shown on the figure ?? represents the two methods to design pixel. The first one, corresponding to the left part of the circuit diagram, consists to reinitialise the collection diode's voltage to a reference voltage thanks to a *reset* transistor, denoted M1 on the diagram. This method works in two steps. Firstly, the M1 transistor is closed and the charge of the equivalent capacitor C_d associated to the junction P-N, represented by a diode on the diagram, is slowly decreasing because of the diode's

leakage current. During this phase, the pixel is sensitive and is read. After a time interval equivalent to the integration time of the sensor, the transistor M1 is opened to recharge C_d to its initial voltage. During this time, the pixel is not sensitive. While M1 is used for the reset, M2 is used as a pre-amplifier of the signal created by the diode and M3 link up the voltage to the output of the circuit. Although this compensation method is fast, it generates a dead time for detection between two readings.

The *self-biased pixel design* method using a p-n junction, symbolised by a diode mounted in the other direction, in the N-well coupled to the collection diode but mounted in the other way to absorb the leakage current. Using a forward p-n junction has the advantage to avoid any dead-time because the diode's leakage current is continuously compensated by the second diode. While no particle is crossing the sensor, there is an equilibrium between the leakage and recharge current. When a particle is crossing the sensor, the charges are collected by the pixel, leading to a discharge of the diode's capacitor C_d , which is followed by a recharge to reach again the equilibrium. Nevertheless, the recharge procedure should be slower than the integration time to be able to detect physics signal during detection. Indeed, when the recharge is too fast, the physics signal is masked and the passage of particle will never be notified. Even if the time interval to recharge the capacitor C_d is set properly, an important charge collection per pixel could disturb the recharge phase and the pixel will reach a stable level again only a long time interval of the order of 10 ms.

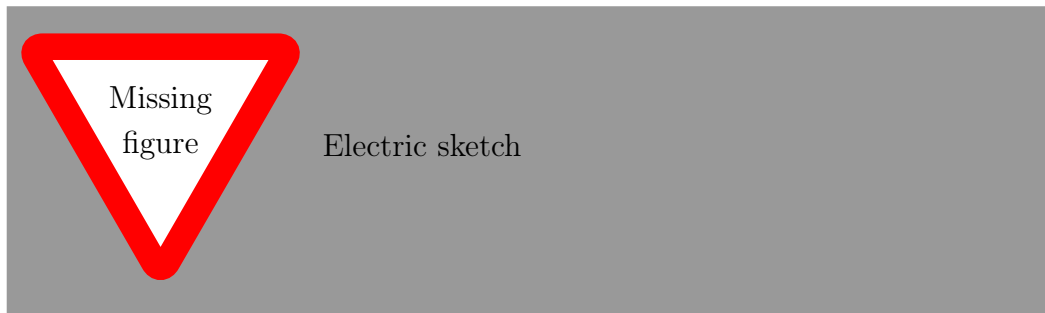


Figure 4.4 – Two different architectures of pixel. The left one is a pixel of type 3T, whereas the right one is a self-biased one.

TALK ABOUT READOUT

As discussed earlier in the architecture of MAPS, for a non-depleted epitaxial layer, the charge carriers are thermally diffused to the pixels. The time to collect these charges in a pixel is ~ 100 ns, setting a maximal limit to

read the signal. Unfortunately, the readout is limited by other factors such as the pixel occupancy or the time needed to obtain information of all the pixels. Faster is the sensor, more important is the power consumption of the electronic. So the design of the sensor is limited by the performance we can reach. To reduce integration time, bigger pixel size can be used, therefore impacting the pointing resolution.

The first sensors developed were using the analog output, but the time integration reachable is too high for a ILC purpose (~ 1 ms). By reading only the fired pixels,

- diffusion: charge collection is done in 100 ns for non-depleted sensor
- Compromise between pixel pitch, power consumption and integration time
- Analog sensors limited in integration time
- Digital output with zero suppression is decreasing data band-with and readout
- Rolling-shutter: read one line one the previous line is treated. $=>$ One row read in 100 ns independently of the number of columns
- Presentation of SUZE

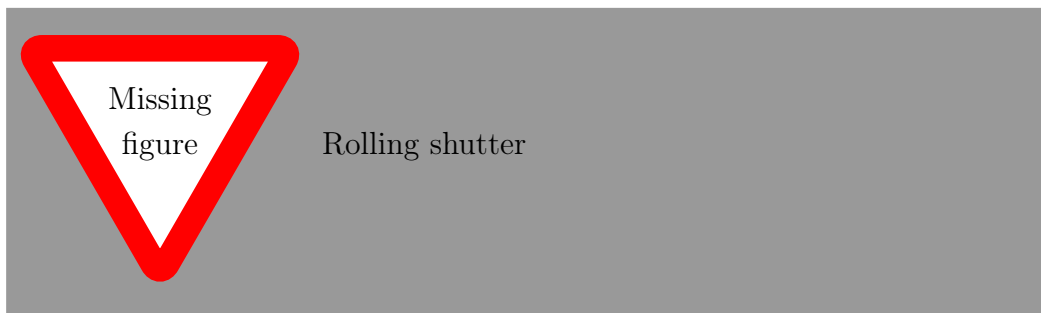


Figure 4.5 – Parallel column readout.

TALK ABOUT NOISE Fixed Pattern Noise (FPN) and Temporal Noise (TN)

Noise during reset : correspond to TN, only for 3T pixels induced by

Noise during integration : shot noise, leakage current fluctuations, leakage current (process, temperature, architecture)

Noise during readout

Correlated Double Sampling : done inside a pixel or at the end of a column. Remove FPN and reset noise

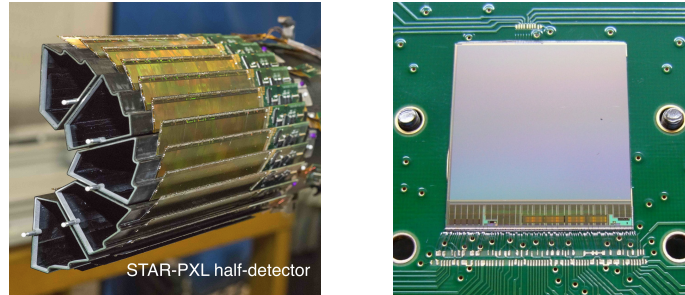
The chapter 5 describes the steps to characterise the fixed pattern noise and temporal noise.

4.3.4 State of the art in high energy physics

The PICSEL group has developed sensors, called **ULTIMATE**, for the **STAR experiment at Brookhaven National Laboratory**. They are based on Minimum Ionizing MOS Active pixel sensor (MIMOSA)-28 sensors and are integrated into the vertex detector. The figure 4.6 is showing a half-section of the STAR vertex detector (subfigure 4.6a) and a MIMOSA-28 bounded on a PCB. The choice for this technology was made because of their characteristics. Indeed, the thickness of a sensor is around $50 \mu\text{m}$ in order to minimise the multiple scattering of particles. The matrix is made of roughly 9×10^5 pixels, corresponding to 960 columns and 928 rows for a pitch of $20.7 \times 20.7 \mu\text{m}^2$. The sensitive area is $19.7 \times 19.2 \text{ cm}^2$. They have a binary output integrating a zero suppression technology (SUZE) and the integration time of the whole matrix is $200 \mu\text{s}$. Thanks to this architecture, the sensors can reach a particle detection rate of $10^6 \text{ particles/cm}^2/\text{s}$. Finally, their power consumption is lower or equal to 150 mW/cm^2 . The spatial resolution obtained for ULTIMATE is less than $4 \mu\text{m}$.

An older version of the MIMOSA-28, based on the same architecture is currently used on the PLUME ladder: MIMOSA-26. Contrary to his brother, the matrix contains roughly 7×10^5 pixels, distribute on 1152 columns and 576 rows. The pixels are scared with a pitch of $18.4 \mu\text{m}$ and the sensitive area is $21.2 \times 10.6 \text{ cm}^2$. They also have a binary output integrating a zero suppression mode but the integration time of the whole matrix is $115.2 \mu\text{s}$. The architecture of a MIMOSA-26 is represented on figure ???. The power consumption is $1.1 \mu\text{W/pixel}$. These sensors are equipping the telescope planes at DESY and CERN.

REF to a paper



(a) Half part picture of the pixel vertex detector at STAR.

(b) ULTIMATE chip bounded on a PCB. The top wire bounds are used for a slow analog output dedicated to lab test, while the bottom ones are the wire bounds which control and read the sensor.

Figure 4.6 – Pictures of the STAR vertex detector and an ULTIMATE chip

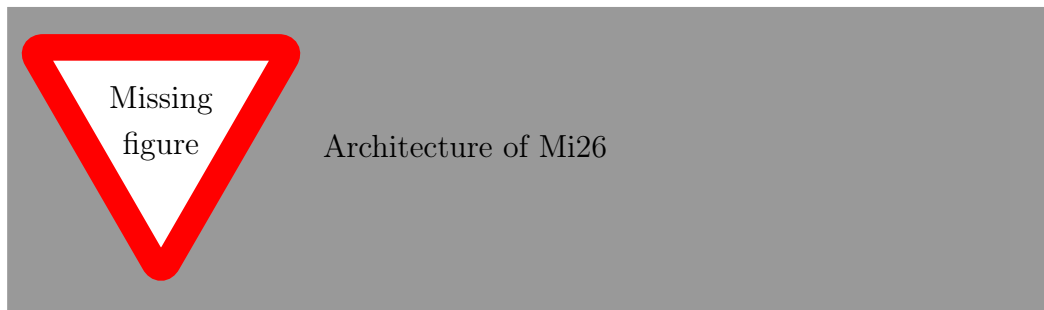


Figure 4.7 – Layout of the MIMOSA-26 matrix.

Chapter 5

Electrical Validation and laboratory testing

This chapter is introducing the steps to characterise and validate a sensor in lab before testing it in real conditions.

- Describe bench
- Describe control of a sensor
- Describe output of Mi-26

5.1 Mechanical check

- Check positioning matrix defect (crack)
- Check wire bounds
- Check alignment

5.2 Electrical validation

- Check consumption
- Check JTAG control
- Check Output

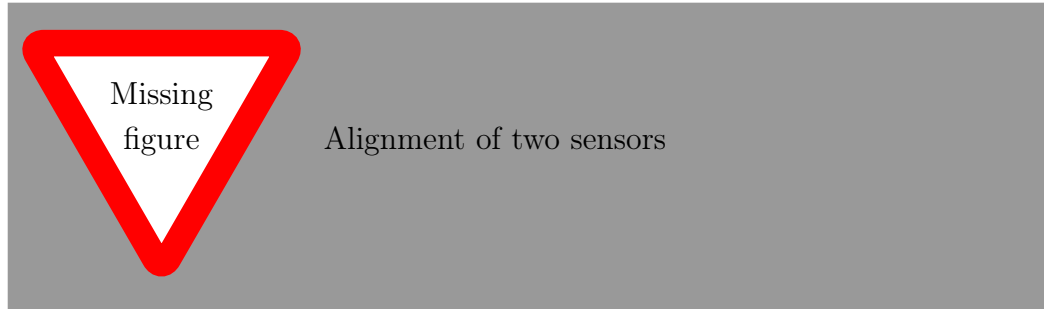


Figure 5.1 – Alignment check made with a microscope.

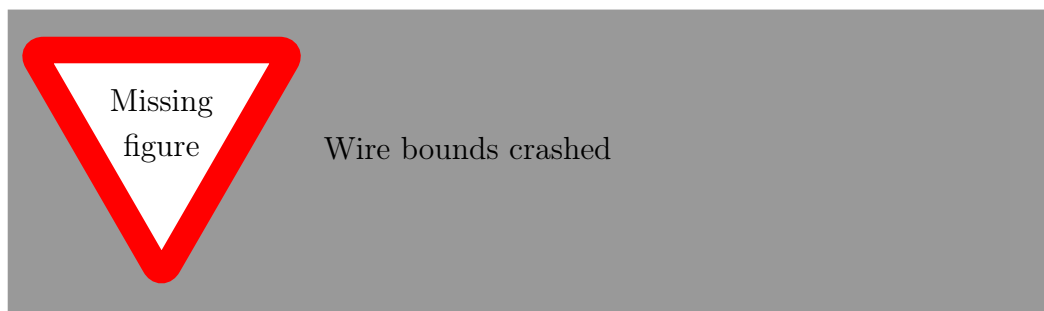


Figure 5.2 – One has to be careful!

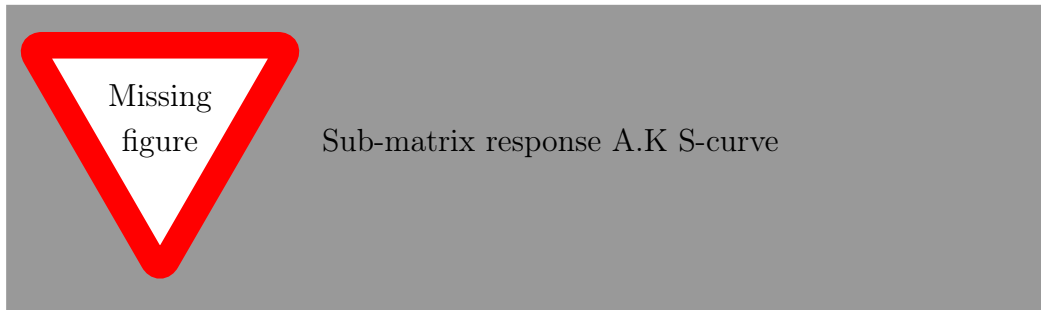


Figure 5.3 – Sub-matrix response

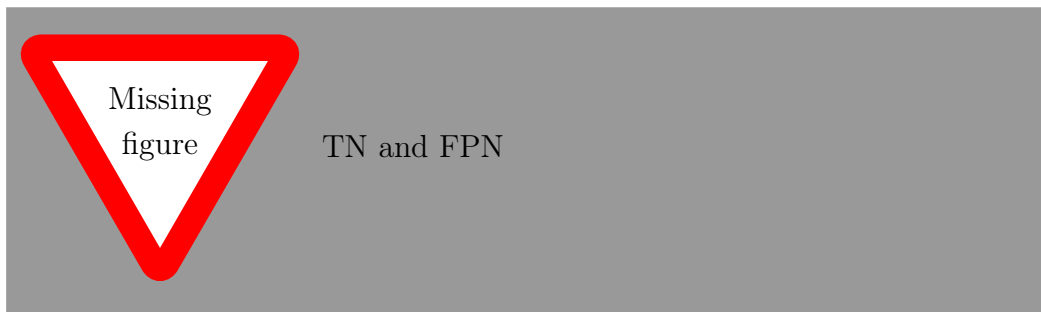


Figure 5.4 – TN and FPN

5.3 Noise estimation

- Describe steps
- Describe analysis
- FHR with normal acquisition

5.4 Cluster

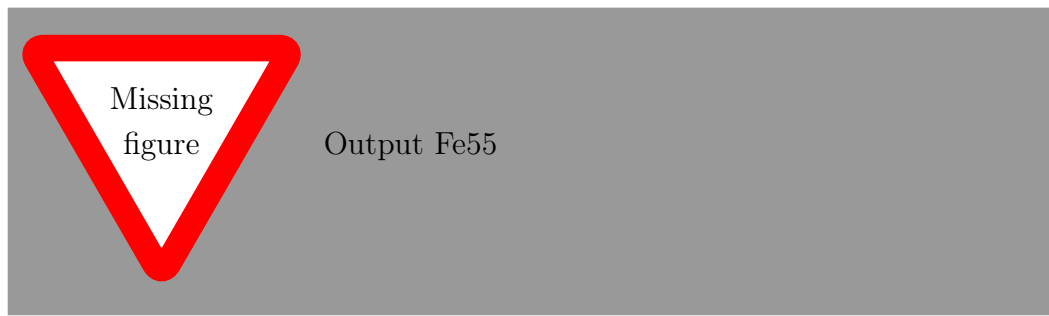


Figure 5.5 – Output of 10k events acquisition with a Fe55 radiation source.

Chapter 6

Test beam analysis

- 6.1 Experimental set-up
- 6.2 Deformation studies
- 6.3 Benefits of double-point measurements

Acronyms

AHCAL Analogue HCAL. [33](#)

APS Active Pixel Sensor. [45](#)

ASIC Application-Specified Integrated Circuit. [45](#)

BDS Beam Delivery System. [23](#)

CCD Charged Coupled-Device. [44](#)

CLIC Compact LInear Collider. [22](#)

CMOS Complementary Metal Oxide Semi-conductor. [41](#)

DAQ Data AcQuisition. [46](#)

DC Direct-current. [23](#)

DEPFET Depleted P- Channel Field Effect Transistor. [45](#)

ECAL Electromagnetic CALorimeter. [31](#)

EM electromagnetic interaction. [3](#)

ETD End-cap Tracking Detector. [31](#)

FPCCD Fine Pixels Charged Coupled-Device. [44](#)

FPN Fixed Pattern Noise. [53](#)

FTD Forward Tracking Detector. [31](#)

GRPC Glass Resistive Plate Chamber. [33](#)

- HCAL** HAdronic CALanalogue HCALorimeter. [33](#)
- ILC** International Linear Collider. [22](#)
- ILD** International Large Detector. [19](#)
- IP** interaction point. [25](#)
- IR** interaction region. [23](#)
- LHC** Large Hadron Collider. [19](#)
- LHCAL** Low angle Hadron CALorimeter. [33](#)
- MAPS** Monolithic Active Pixel Sensor. [33](#)
- MIMOSA** Minimum Ionizing MOS Active pixel sensor. [54](#)
- MIP** Minimum Ionizing Particle. [49](#)
- PFA** Particle Flow Algorithm. [28](#)
- PLUME** Pixelated Ladder with Ultra-low Material Embedding. [46](#)
- RTML** Ring To the Main Linac. [24](#)
- SDHCAL** Semi-Digital HCAL. [33](#)
- SET** Silicon External Tracking. [31](#)
- SiD** Silicon Detector. [28](#)
- SIT** Silicon Internal Tracker. [31](#)
- SM** Standard Model. [2](#)
- SRF** Superconducting Radio-Frequency. [21](#)
- TN** Temporal Noise. [53](#)
- TPC** Time-Projection-Chamber. [28](#)
- VXD** Vertex Detector. [29](#)

Bibliography

- [1] Georges Aad et al. Observation of a new particle in the search for the Standard Model Higgs boson with the ATLAS detector at the LHC. *Phys. Lett.*, B716:1–29, 2012.
- [2] R. Appleby, L. Keller, T. Markiewicz, A. Seryi, R. Sugahara, and D. Walz. The International Linear Collider Technica. 3, 2006.
- [3] H Baer, T Barklow, K Fujii, Y Gao, and a Hoang. [1306.6352] The International Linear Collider Technical Design Report - Volume 2: Physics. ... preprint *arXiv:13066352*, 2, jun 2013.
- [4] M. Battaglia. Vertex tracking at a future linear collider. *Nucl. Instruments Methods Phys. Res. Sect. A Accel. Spectrometers, Detect. Assoc. Equip.*, 650(1):55–58, sep 2011.
- [5] T. Behnke, J. E. Brau, B. Foster, J. Fuster, M. Harrison, J. P. Paterson, M. Peskin, M. Stanitzki, N. Walker, and H. Yamamoto. ILC Technical Design Report Volume 1: Executive Summary. *ILC Tech. Des. Rep. Vol. 1 Exec. Summ.*, 1:1–60, 2013.
- [6] Ties Behnke. The international linear collider. *Fortschritte der Phys.*, 58(7-9):622–627, 2010.
- [7] Constantino Calancha Paredes, A Dubey, H Ikeda, A Ishikawa, S Ito, E Kato, A Miyamoto, T Mori, H Sato, T Suehara, Y Sugimoto, and H Yamamoto. Progress in the development of the vertex detector with fine pixel CCD at the ILC.
- [8] Serguei Chatrchyan et al. Observation of a new boson at a mass of 125 GeV with the CMS experiment at the LHC. *Phys. Lett.*, B716:30–61, 2012.
- [9] Deutsches Elektronen-synchrotron Desy and Hamburg Germany. A review of e+ e- Linear Colliders. 22:529–539, 1988.

- [10] F. Englert and R. Brout. Broken Symmetry and the Mass of Gauge Vector Mesons. *Physical Review Letters*, 13:321–323, August 1964.
- [11] E. Fermi. An attempt of a theory of beta radiation. 1. *Z. Phys.*, 88:161–177, 1934.
- [12] R. P. Feynman and M. Gell-Mann. Theory of the fermi interaction. *Phys. Rev.*, 109:193–198, Jan 1958.
- [13] Steven Green, John Marshall, Mark Thomson, and Boruo Xu. Cambridge linear collider group - home page. <http://www.hep.phy.cam.ac.uk/linearcollider/calorimetry/>.
- [14] Peter W. Higgs. Broken symmetries and the masses of gauge bosons. *Phys. Rev. Lett.*, 13:508–509, Oct 1964.
- [15] ICFA. Final International Technology Recommendation Panel Report. (September), 2004.
- [16] T. D. Lee and C. N. Yang. Question of Parity Conservation in Weak Interactions. *Physical Review*, 104:254–258, October 1956.
- [17] Yiming Li, Chris Damerell, Rui Gao, Rhorry Gauld, Jaya John John, Peter Murray, Andrei Nomerotski, Konstantin Stefanov, Steve Thomas, Helena Wilding, and Zhige Zhang. ISIS2: Pixel Sensor with Local Charge Storage for ILC Vertex Detector. page 11, jun 2010.
- [18] Ronald Lipton. Muon Collider: Plans, Progress and Challenges. page 6, apr 2012.
- [19] O. Markin. Backgrounds at future linear colliders. feb 2014.
- [20] K. A. Olive et al. Review of Particle Physics. *Chin. Phys.*, C38:090001, 2014.
- [21] Adrian Signer. ABC of SUSY. *Journal of Physics G: Nuclear and Particle Physics*, 36(7):073002, jul 2009.
- [22] C. S. Wu, E. Ambler, R. W. Hayward, D. D. Hoppes, and R. P. Hudson. Experimental Test of Parity Conservation in Beta Decay. *Physical Review*, 105:1413–1415, February 1957.